Rainfall stable water isotope variability in coastal southwestern Western Australia and its relationship to climate on multiple timescales

Alan D Griffiths[1,2], Pauline C Treble[1,3], Pandora Hope[4], Irina Rudeva[4,5]

[1]ANSTO, Lucas Heights, NSW, Australia
[2]Centre for Atmospheric Chemistry, University of Wollongong, Wollongong NSW, Australia
[3]School of Biological, Earth and Environmental Sciences, UNSW, Sydney NSW, Australia
[4]Australian Bureau of Meteorology, Melbourne, Victoria, Australia
[5]P.P. Shirshov Institute of Oceanology, Moscow, Russia

Key Points:

- Precipitation δ^{18}O variability is driven primarily by rainfall intensity in southwestern Western Australia
- Interannual δ^{18}O variability is strongly influenced by the largest rainfall events of the year
- Humidity during evaporation drives deuterium excess variability at a daily, but not interannual, timescale

Corresponding author: Alan Griffiths, `Alan.Griffiths@ansto.gov.au`

Abstract

The factors driving variability in rainfall stable water isotopes (specifically $\delta^{18}O$ and deuterium excess, $d = \delta^2H - 8\,\delta^{18}O$) were studied in a 13-year dataset of daily rainfall samples from coastal southwestern Western Australia (SWWA). Backwards dispersion modelling, automatic synoptic type classification, and a statistical model were used to establish causes of variability on a daily scale; and predictions from the model were aggregated to longer temporal scales to discover the cause of variability on multiple timescales. Factors differ between $\delta^{18}O$ and d and differ according to temporal scale. Rainfall intensity, both at the observation site and upwind, was most important for determining $\delta^{18}O$ and this relationship was robust across all time scales (daily, seasonal, and interannual) as well as generalizing to a second observation site. The sensitivity of $\delta^{18}O$ to rainfall intensity makes annual mean values particularly sensitive to the year's largest events. Projecting the rainfall intensity relationship back through ~ 100 years of precipitation observations can explain ~ 0.2–0.4‰ shifts in rainfall $\delta^{18}O$. Twentieth century speleothem records from the region exhibit signals of a similar magnitude, indicating that rainfall intensity should be taken into account during the interpretation of regional climate archives. For d, humidity during evaporation from the ocean was the most important driver of variability at the daily scale, as well as explaining the seasonal cycle, but source humidity failed to explain the longer-term interannual variability.

Plain Language Summary

In cave deposits, as with several other natural systems, the relative abundance of the heavy isotopes oxygen-18 and deuterium can be used to determine past changes in climate. This is because the isotopic composition of these systems is linked to that of rainfall, while the abundance of heavy isotopes in rainfall is driven by climate parameters such as temperature and rainfall characteristics. For this to be possible, the factors which drive rainfall isotopic variability need to be well known. This study uses a 13-year data set of daily rainfall samples from coastal southwestern Western Australia to better understand isotopic variability for this region. Oxygen-18 variations here are driven mainly by rainfall intensity (the amount of rain each day) both according to measurements at the site and upwind simulations. Deuterium excess, a second order parameter which is often linked to conditions in the evaporation source region, was well-predicted by source region humidity at the daily scale but not when aggregated to annual totals. The relationship between rainfall intensity and oxygen-18 appears to be important over the 20th century, based on a comparison between observed rainfall and a cave record.

1 Introduction

In systems where material is sequestered from the environment, for instance during speleothem growth or groundwater infiltration, the stable isotope ratios $\delta^{18}O$ and δ^2H act as markers of environmental change. Speleothems, that is cave decorations such as stalagmites and flowstones, record changes in the oxygen isotopic composition as they grow, and these changes can in turn be linked to changes in rainfall isotopic composition (Lachniet, 2009; Orland et al., 2009; Z. Zhang et al., 2018). Karst regions occur throughout the midlatitudes (Chen et al., 2017) meaning that cave records can be used to infer past changes in certain aspects of the hydrological cycle, in areas where this is not achievable using materials such as coral and ice (Treble, Chappell, et al., 2005; Lorrey et al., 2008; Fohlmeister et al., 2012; McCabe-Glynn et al., 2013; H. Zhang et al., 2018). Speleothem use is widespread, with the SISALv2 database alone containing 691 time-series of $\delta^{18}O$ in speleothem calcite (Comas-Bru et al., 2020).

The ratio of deuterium to hydrogen, δ^2H, also reflects changes in hydrological processes. Even though it is not directly preserved in speleothem carbonite, calcareous speleothems

nevertheless record the history of δ^2H in infiltrating water because of the formation of fluid inclusions within the speleothem which trap enough water for isotopic analysis (Vonhof et al., 2006; van Breukelen et al., 2008). Alternatively, groundwater can be sampled and dated to obtain a low-resolution record of both δ^{18}O and δ^2H (Priestley et al., 2020).

Interpreting these records, of oxygen-18 in calcite and deuterium in fluid inclusions, relies on an understanding of how climatic and atmosphere processes drive isotope variability in rainfall. At the laboratory scale, this is well understood. In a closed system, heavier isotopes are concentrated in the more condensed phase according to the temperature-dependent equilibrium fraction factor (Horita & Wesolowski, 1994; Majoube, 1971). In well-controlled conditions where diffusive transport is important, the difference in molecular diffusivity between isotopologues (Merlivat, 1978b) leads to quantitatively-predictable kinetic fractionation. In the climate system, however, precisely which climatic and atmospheric processes emerge with the strongest link to isotopic variations is less clear and differs between regions.

Towards the poles, over long time scales, oxygen and hydrogen isotopes in ice have been used as an indicator of temperature (Brook & Buizert, 2018; Jouzel et al., 2007); whereas tropical rainfall isotopes have classically been thought of as being controlled by precipitation amount (Dansgaard, 1964). Other factors are also important, though, some of which are location-dependent. In the tropics, these factors include the degree of convective organization (Moerman et al., 2013) or monsoon activity (Okazaki et al., 2015). In both the tropics and midlatitudes, the type of precipitation (Aggarwal et al., 2016) and atmospheric residence time (Aggarwal et al., 2012) are important. In studies from the midlatitudes, the moisture source (Krklec & Domínguez-Villar, 2014) and, more generally, the airmass history (Deininger et al., 2016; Good et al., 2014) have been identified as drivers of isotopic variability.

One way to simplify the analysis of many individual factors, and potentially making interpretation more robust or straightforward, is to examine the link between the type of synoptic-scale weather system and water isotopes in precipitation. Using this approach in Southern Australia (Barras & Simmonds, 2008, 2009; Treble, Budd, et al., 2005; Guan et al., 2013), and elsewhere (Lykoudis et al., 2010; Farlin et al., 2013; Tyler et al., 2016; Wang et al., 2017; Schlosser et al., 2017), has indeed revealed that an association exists. It arises because several of the factors mentioned above systematically differ between synoptic types.

This study is concerned with southwestern Western Australia (SWWA) in the Southern Hemisphere midlatitudes. Here, δ^{18}O values in speleothem records (Treble, Chappell, et al., 2005) have low frequency variations that are likely to be linked to climate, but a robust understanding of the mechanism is incomplete. Treble, Chappell, et al. (2005) showed that the stable water isotopes measured in SWWA daily rainfall samples, over a one-year study period, are associated with rainfall intensity, but other drivers may also play a role. It is also unclear whether the intensity dependence holds over longer time periods. An understanding of these drivers is particularly important for this region; winter rainfall here has dropped significantly since the 1970s (Bates et al., 2008) and placing this in the context of the region's long-term natural variability is important for fully understanding the change. This is a challenging task because of the region's strong internal variability, demonstrated in climate models (Cai et al., 2005; England et al., 2006), combined with a short ($\sim$100 yr) instrumental record (Haylock & Nicholls, 2000).

There are several approaches for determining climate variability using paleoclimate records or reconstructions. Changes in rainfall have been inferred from distant measurements of snow accumulation (Zheng et al., 2021), which is possible because of an anti-correlation between SWWA May–October rainfall and snowfall at Law Dome, Antarctica (van Ommen & Morgan, 2010). Speleothem records, an in situ climate proxy, are found in caves which develop in Tamala Limestone (Geoscience Australia & Australian

Stratigraphy Commission, 2017), an eolian carbonate deposited in the Middle to Late Pleistocene, ∼10–250 ka before present (Smith et al., 2012). Tamala Limestone is extensively distributed along several hundred kilometers of the Western Australian coastline (Fig. 1). Meanwhile, groundwater from the confined aquifers of the Perth Basin (Priestley et al., 2020) has been interpreted as a low-resolution record of infiltration. Both speleothem and groundwater records would benefit from a better understanding of the climate drivers of stable water isotopes.

The purpose of this paper, then, is to investigate the factors which influence the abundance of stable water isotopes (^{2}HHO, $H_2^{18}O$) in a modern 13 yr record of SWWA rainfall, taking into account day-to-day variations in synoptic types, upstream conditions, and site parameters. In particular, our goal is to identify factors which are important both at the daily, seasonal, and annual scales. This is most relevant to understanding speleothem records from the region, although we expect the measurements to be more widely useful.

The remainder of this paper is organized as follows: Sect. 2 describes the characteristics of the study region; Sect. 3 introduces the methods used in this study, including a Lagrangian trajectory model and statistical methods; Sect. 4 describes the main results and illustrates links between water isotopes and their drivers; and Sect. 5 compares our results with the literature, tests the ability of our interpretation to generalize to another site, as well as summarizing implications for speleothem record interpretation.

2 Regional setting

The coastal region of southwestern Western Australia (SWWA, Fig. 1), has an annual rainfall of more than 750 mm making it a wet and productive region in comparison to the arid inland. The region is too warm for snow, so precipitation falls as rain and this is mostly during the cooler months of May–October (Bates et al., 2008, Fig. S1). The total cool-season rainfall is closely related to the number of fronts which cross the coast, which in turn is coupled to the strength and extent of the Hadley-Walker circulation (Rudeva et al., 2019). Along the coastline south of Perth, about 50% of winter rainfall is associated with fronts, which can be accompanied by thunderstorms (Pepler et al., 2020), 20% with cutoff lows (low pressure systems formed at upper tropospheric levels), and the remainder with warm troughs and other synoptic systems (Pook et al., 2012). Further inland, the proportion of frontal rainfall is lower, and the climate is dryer. Other studies, although differing in how synoptic systems are defined (Hope et al., 2014), have generally classified rainfall-bearing systems into similar synoptic types (Raut et al., 2014; Hope et al., 2006) and agree on the importance of frontal rainfall during the rainy winter season. In summer, when the subtropical ridge lies over the region, monthly rainfall of 20 mm or less is typical and frontal rainfall makes up a smaller proportion of the total. Instead, rainfall comes from a mixture of thunderstorms, extratropical cyclones, (Pepler et al., 2020) and warm troughs (Raut et al., 2014). Also more likely during summer are the rare, but potentially extreme, events from ex-tropical cyclones (Foley & Hanstrum, 1994).

As well as having a pronounced seasonal cycle, the region's rainfall has changed on interannual to decadal timescales. Since 1970, the water inflow to Perth's dams has decreased by half (Power et al., 2005), due to the combined effect of reduced winter rainfall and increased evaporation. The rainfall intensity distribution has also changed over the instrumental period, but with differences between stations within SWWA (Philip & Yu, 2020). A number of studies, reviewed by Dey et al. (2019), show the rainfall decrease, in winter, is associated with a change in regional circulation including a poleward shift in westerly winds. The resulting decrease in the frequency of strong fronts (Raut et al., 2014) has been related to a significant warming of the Southern Hemisphere troposphere

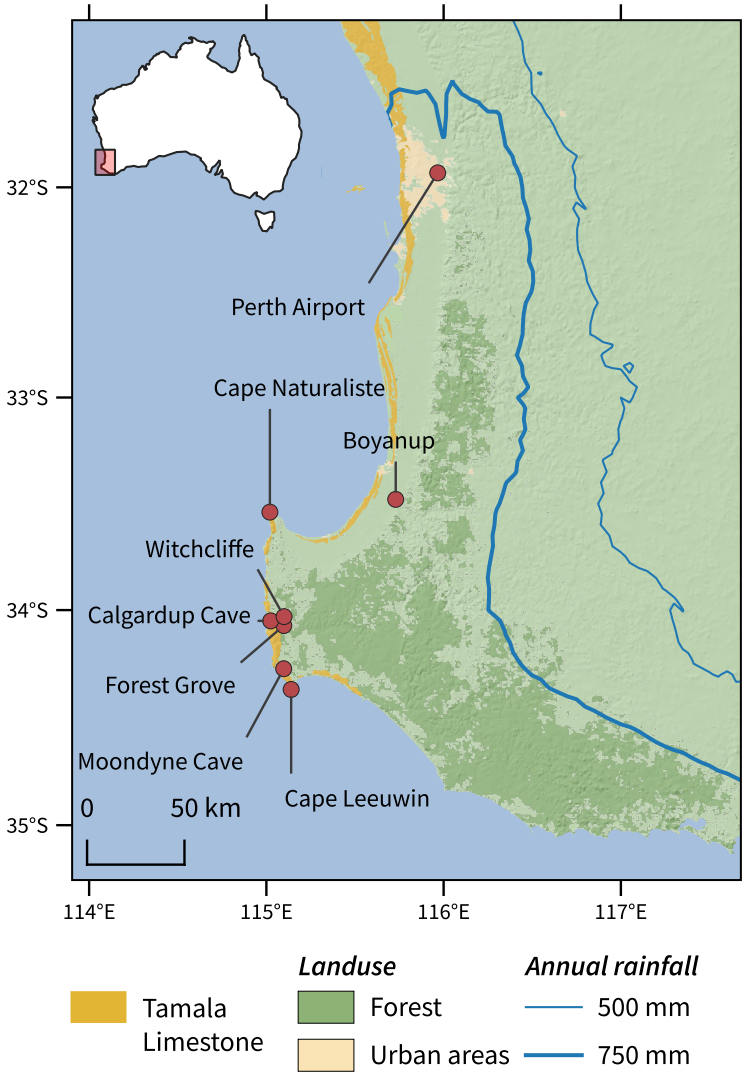

Figure 1. Southwestern Western Australia (SWWA) and locations referenced in the text with: the distribution of Tamala Limestone (a karstic eolianite that occurs along the coast; Geoscience Australia, 2012); land cover (Paget, 2008); and annual mean rainfall (Australian Bureau of Meteorology product IDCJCM004).

south of 30°S followed by a decrease in the strength of the jetstream, which, in turn, decreases the instability and makes the formation of synoptic disturbances less likely (Frederiksen & Frederiksen, 2007). This is in agreement with a recent study by Lucas et al. (2021), who described a reduction in the intensity of the upward midlatitude circulation branch in the Southern Hemisphere at 30°S. Climate model projections indicate that the drying trend will continue (Bates et al., 2008; Raut et al., 2016).

3 Methods and data

3.1 Rainfall sampling

Rainfall samples were collected from the Calgardup Cave visitors center within a forested nature reserve 23 km from the coast (34.0499°S, 115.0246°E, 70 m ASL, Fig. 1). Samples were collected in a rain gauge consisting of a 203 mm diameter circular funnel draining into a graduated cylinder. The top of the rain gauge was approximately 0.3 m above the ground and within a small clearing; nearby vegetation was kept clear of the gauge. The gauge was checked daily at 0900 local time (0100 UTC for most of the record, however Western Australia observed daylight saving time during the summers of 2006–2009) and on days with at least 2 mm of rainfall a sample was collected by filling a 12 ml amber glass bottle completely to the rim. The sample bottle was sealed using a polypropylene lid with Teflon tape placed around the thread to improve the seal. Samples were kept refrigerated at 3 °C until analysis. For this study, measurements were included from the years 2006–2018 to avoid including partial years. Occasionally, observers sampled rainfall on days with $<$ 2 mm of rainfall, and these samples were excluded from analysis. In addition, one outlier was excluded. This was recorded on 21 April 2010 with an anomalously high δ^{18}O of -1.2‰ with 52 mm of rainfall, compared to an expected value of about -5‰ for this amount of rainfall. Three rain-days later a sample was anomalously low (-5.0‰ with 4.1 mm of rainfall), so it is possible that samples were mislabeled.

Isotopes are reported in terms of the isotopologue ratios, R, of oxygen–18 ($H_2^{18}O/H_2O$) and deuterium ($^2HHO/H_2O$) relative to Vienna Standard Mean Ocean Water (VSMOW; IAEA, 2006) in rainwater. We use delta notation where $\delta = R/R_{\mathrm{VSMOW}} - 1$, with δ^{18}O and δ^2H representing the two isotopologues. Data up to March 2012 were previously published (Treble et al., 2013). New data reported here were obtained using a Picarro L2120-I cavity ring-down spectroscopy analyzer at ANSTO (reported accuracy of ±1.0 ‰ for δ^2H and ±0.1 ‰ for δ^{18}O). All samples were filtered prior to analysis and data were reported against in-house standards calibrated to VSMOW/VSMOW2 and SLAP/SLAP2.

Because δ^{18}O and δ^2H are strongly correlated, we present δ^{18}O results along with deuterium excess, d, a second-order parameter which characterizes the departure of δ^2H from a linear relationship with δ^{18}O. We follow the most common definition (Dansgaard, 1964) where

$$d = \delta^2\mathrm{H} - 8\,\delta^{18}\mathrm{O}. \tag{1}$$

Defined this way, d is approximately conserved during Rayleigh distillation, provided that the ambient temperature is close to 31°C and that Rayleigh distillation does not proceed too far. Although this is a conventional approach, making our results simple to compare with other studies, it is nevertheless possible for equilibrium processes to change d and other definitions have been proposed, as discussed by Dütsch et al. (2017). At colder temperatures, Rayleigh distillation tends to decrease d, as it proceeds because the equilibrium fraction factors depend on temperature (Horita & Wesolowski, 1994). Since the heavy isotopes are depleted by Rayleigh distillation, the effect is to produce a positive correlation between d and δ^{18}O at cool temperatures. This trend reverses, however, once Rayleigh distillation proceeds far enough (less than about 10% of vapor remaining) meaning that Rayleigh theory predicts that dry mid-tropospheric air has low δ^{18}O and high d, in general agreement with observations (Sodemann et al., 2017).

Rainfall isotope data are also presented from the Perth Airport Global Network of Isotopes in Precipitation (GNIP) sampling point, 250 km north of Calgardup Cave, where rainfall is accumulated monthly for isotopic analysis (Hollins et al., 2018). Approximately 7 km further inland from Calgardup Cave, there are two automatic weather stations operated by the Australian Bureau of Meteorology (BoM) at sites 9746 (Witchcliffe) and 9547 (Forest Grove). Rainfall measurements are taken from these sites, as well as the more distant sites: 9503 (Boyanup) and 9519 (Cape Naturaliste).

In this paper, the amount of rainfall collected each day is called the 'rainfall intensity', in contrast to 'rainfall total' which is the accumulated rainfall over a longer period. Where averages of δ^{18}O and d are computed, these are weighted by rainfall amount unless noted otherwise.

3.2 Source region diagnostic

Several upstream parameters, chosen because of their potential to affect δ^{18}O and d, were diagnosed using Lagrangian dispersion models. Models were used to compute a backwards plume, or retroplume, from Calgardup Cave on each day with > 2 mm of rainfall. Backwards plumes are a more realistic generalization of backwards trajectories, with advantages discussed by (Stohl et al., 2002). Lagrangian diagnostics have been widely and successfully used in studies of water isotopes (Pfahl & Wernli, 2008, 2009; Sodemann et al., 2008, e.g.) including the use of backwards dispersion models (Good et al., 2014). Quantities related to the evaporation source region were diagnosed from the source-receptor matrix (Seibert & Frank, 2004) weighted by the instantaneous evaporation rate.

In this study, two sets of backwards plumes were generated. The primary set used FLEXPART version 9.0 (Stohl et al., 2002) with subgrid convective mixing (Forster et al., 2007) and wind fields from the ERA-Interim reanalysis (Dee et al., 2011). A second set of backwards plumes was generated using FLEXPART-WRF version 3.1 (Brioude et al., 2013), forced with a regional atmospheric simulation generated by the Weather Research and Forecasting model version 3.5.1 (WRF Skamarock & Klemp, 2008). The WRF model was forced by the CFSR reanalysis (Saha et al., 2010), and configured with an outer domain which was large enough to contain the backwards plume for approximately 120 h. The second set of plumes was used to verify that the main findings could be replicated and are not discussed further.

Three of the uncertainties in the approach are that: the time of rainfall is only known to within a 24 h sampling window; the appropriate height for beginning the backwards plume has to be estimated; and the error in the plume grows as the model is integrated further back in time. After some experimentation, the beginning time was taken from the time in the WRF simulation with the largest rain rate, and the starting height was taken to be the cloud base in WRF, estimated at the height when relative humidity reaches 80%. Then, to verify that the model indeed produces a useful diagnostic, we checked the correlation between d and humidity relative to saturation at the sea surface temperature, h_s, as a function of back trajectory length. This is a useful diagnostic because d, in vapor, and h_s, at the evaporation site, are strongly correlated (Pfahl & Wernli, 2008) and we assume that d will be approximately conserved during the conversion of water vapor into clouds and then rainfall.

The correlation between d and h_s grows as the backwards plume increases in duration up to about 48 h, but with no further improvement beyond this point (Fig. S2). This indicates that both dispersion models have some skill at determining the evaporation conditions at the moisture source, at least up to 48 h before rainfall.

3.3 Synoptic classifications

On each day, the synoptic type was classified with a Self Organizing Map (SOM), using SOM-PAK (Kohonen et al., 1996), following the approach described by Hope et al. (2006). Synoptic types were derived from the 1200 UTC mean sea level pressure (MSLP) anomaly fields of the ERA-Interim reanalysis on a 0.75° latitude/longitude grid in the region 90–130°E, 50–15°S. The SOM is an unsupervised classification method, producing synoptic types that are arranged in a two-dimensional grid. The arrangement of types into a grid, where similar synoptic types are arranged close to each other, is the main way in which the SOM differs from other statistical classification techniques (Philipp et

al., 2016). Synoptic classification was only applied to the rainy months (April–October), due to the presence of seasonally persistent features in the surface pressure field associated with the meridional movement of the subtropical high pressure ridge. Training was performed using data from the years 1979–2018 and grid cells were weighted by area.

In addition to the SOM classifications, fronts were detected in the reanalysis fields and used as an aid to interpret the SOM classifications. The position of fronts was found using the wind shift method (Simmonds et al., 2011) based on ERA-Interim 3-hourly 10 m wind fields. This is a straightforward method which is applicable to SWWA (Hope et al., 2014). It does not produce spurious fronts along the coastline, that are often found by a more commonly used methods based on the temperature gradients (Pepler et al., 2020). The wind-based method works well to define meridionally elongated fronts, that are mainly cold fronts, and is particularly well suited for the Southern Hemisphere (Schemm et al., 2015).

3.4 Generalized additive models

To combine information from site measurements, backwards plume, and synoptic type we used Generalized Additive Models (GAMs; Wood, 2017). Separate models were constructed to predict δ^{18}O and d in daily rainfall samples. GAMs, a generalization of linear regression models, allow the relationships between predictor variables and the response variable to be modelled as smooth curves rather than straight lines. In contrast to many nonlinear machine learning techniques, a benefit of using GAMs is that the relationship between predictor and response variables is simple to visualize, making the models readily interpretable.

The GAM implementation was provided by mgcv, a package for R (R Core Team, 2014). Relationships between predictor and response variables are modelled with penalized regression splines in which the smoothness is estimated during the fitting process using restricted maximum likelihood (REML; Wood, 2011), and models used the identity link function. In this implementation, predictors which can be modelled with a linear response are modelled that way, and predictors with insufficient explanatory power are dropped from the model. The mgcv models can also incorporate categorical variables, allowing the synoptic classification to be included within the same framework.

In this study, we also assessed the importance of terms for explaining the observations on different timescales. As well as allowing the models to drop unimportant terms (using REML) we followed a procedure where models were constructed term-by-term. Beginning with an empty model, each candidate term was tested, and the term resulting in the best performing model retained. The search for the best term was then repeated by adding a second term to the model, and so on.

The metric for assessing model performance was the 13-fold cross-validated mean-square error (MSE) applied to daily predictions of δ^{18}O or d. To score a model, one year is held out, and the other years are used to train the model, then the MSE computed on the held-out year, defined as

$$\mathrm{MSE} = \frac{1}{N}\sum_{i=1}^{N}(\hat{y}_i - y_i)^2 \tag{2}$$

where N is the number of observations, y_i is the ith day's observation and $\hat{y}_i$ is the ith day's model prediction. This is repeated for all years in the data set, and the MSE is taken as the average from all the hold-out sets. During model building, terms are added in the order of the greatest reduction in daily cross-validated MSE.

Once the set of models has been obtained, the cross-validated MSE is then recorded for three groupings: 1. the original, daily, data 2. the mean seasonal cycle during the rainy months (April–October); and 3. the annual precipitation-weighted means.

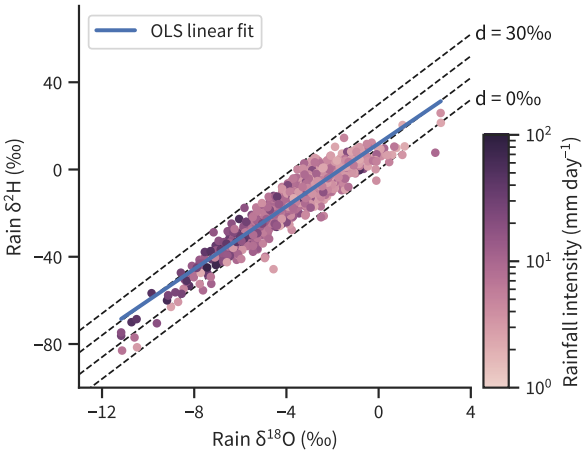

Figure 2. Rainfall δ^{18}O and δ^{2}H measured in daily samples from Calgardup Cave visitors centre coloured by the daily rainfall intensity. For comparison, the global average d in precipitation is about 10‰.

3.5 Modelled precipitation isotopes

In addition to the diagnostic and statistical models described above, we also use output from a prognostic model: a 40 year simulation of IsoGSM (Yoshimura et al., 2008). This is one of several atmosphere general circulation models with water isotope tracers (Risi et al., 2010; Sturm et al., 2005; Schmidt et al., 2007; Lee et al., 2007, e.g.). IsoGSM is forced with the NCEP/DOE Reanalysis and output from the model is available with a horizontal resolution of 2.5°.

At other sites, IsoGSM reproduces daily, monthly, and seasonal variability in water isotope ratios, with more skill at simulating δ^{18}O than d (Yoshimura et al., 2008). At the daily scale, the low accuracy of the model-produced precipitation (that is, the model may not necessarily produce rain on a rainy day) limits the accuracy of predicted water isotopes.

4 Results

Our results include a description of the stable water isotopes in Sect. 4.1–4.3 before moving onto the more interpretive results from statistical and dispersion models in the later sections.

4.1 Daily δ^{18}O, δ^{2}H, and precipitation

Over the 13 year monitoring period (2006-18 inclusive, days with $\geq$2 mm day^{-1} of rainfall) the precipitation-weighted mean (the mean weighted by the daily precipitation amount) δ^{18}O was −4.45‰, d was 15.4‰, and $\delta^{2}H$ was −20.2‰. More than 2 mm of rain fell on an average of 90 days each year, and the mean annual precipitation from these events was 839 mm. The daily isotope samples, when plotted in δ^{18}O ~ δ^{2}H space, are strongly correlated and lie about the so-called local meteoric water line (LMWL; Fig. 2).

There is a tendency for intense rainfall to have lower δ^{2}H and δ^{18}O and for low intensity rainfall to both have high δ^{18}O and, above −2‰, depart from the straight line trend. Deuterium excess for these high δ^{18}O samples tends towards the d = 0 ‰ line,

contrasting to the overall mean d. For comparison, the global meteoric water line (GMWL) of Craig (1961) lies on the $d = 10‰$ line. In common with many Australian sites (Hollins et al., 2018), the slope of the LMWL when calculated with ordinary least-squares (OLS) is lower than the GMWL. The parameters for straight-line fits to the daily rainfall samples are shown in Tab. S1, with both ordinary least-squares and precipitation weighted least squares (WLS, Hughes & Crawford, 2012), although these are not the only options for characterizing the LWML and the slope is dependent on the regression method (Crawford et al., 2014). Taking uncertainty into account, the slope of the LMWL at Calgardup Cave is indistinguishable from the Perth Airport LMWL, but the there is an offset between the two sites since the intercept differs by about two standard deviations. The cause of this offset is explained in Sect. 5.3.

As noted in Sect. 3.1, the temperature-dependence of equilibrium fractionation would lead to an increase in d with $\delta^{18}O$. Here we see the opposite trend, which is indicative of non-equilibrium processes, such as sub-cloud raindrop re-evaporation (Lee & Fung, 2008), becoming relatively more important during light rainfall.

4.2 Seasonal cycle

The composite seasonal cycle of $\delta^{18}O$, d, and rainfall has been published previously for Perth (Hollins et al., 2018; Liu et al., 2010) and the seasonal cycle at Calgardup is broadly similar (shown later in Fig. 8, but also Fig. S1). The similarity is consistent with isotopes at the two sites being driven by similar factors. As shown in these figures, the $\delta^{18}O$ minimum occurs in May or June, which is earlier than the July peak in rainfall. January stands out as an exception with anomalously low–and variable–rainfall $\delta^{18}O$ when compared with the surrounding months, likely because of the occurrence of rare, but intense, rainfall events. The seasonal cycle of d also has a large amplitude, but mirrors $\delta^{18}O$ with a peak in the rainy months. Unlike $\delta^{18}O$, summer variability is not especially pronounced.

4.3 Annual mean time series

Rainfall $\delta^{18}O$, aggregated to annual precipitation-weighted averages, follows an overall decreasing trend, which is present at both Calgardup Cave and Perth as well as in IsoGSM model output (Fig. 3). From 2009 onwards, however, there is no statistically significant trend. Comparison with longer term model output, and earlier data from Perth, (Hollins et al., 2018) indicates that 2006-08 were anomalously high, compared to the long-term average. The annual-mean d (Fig. 3b) shows similar trends at Perth and Calgardup Cave, but the IsoGSM simulations are unable to reproduce the observed trends. There is no consistent trend in d if the first three years are excluded.

On average, annual $\delta^{18}O$ values are 0.61‰ higher at Perth implying a meridional gradient in $\delta^{18}O$ of 0.29 ‰ per degree of latitude. This agrees with a persistent feature of isotope enabled GCMs which simulate a $\delta^{18}O$ maximum over the Indian Ocean north of Perth, near 30°S and under the descending branch of the Hadley Cell, with decreasing values towards the pole (Werner et al., 2011; Lee et al., 2007; Noone & Simmonds, 2002; Risi et al., 2012). The offset between mean values for Perth and Calgardup Cave shows no trend through time, implying that the meridional gradient has remained consistent over the monitoring period.

Annual mean departures from the trend are not consistent between sites (Fig. 3a), suggesting that $\delta^{18}O$ anomalies are related to local processes. At least in part, the low correlation between sites is because annual mean $\delta^{18}O$ is particularly sensitive to the heaviest events of the year, shown by plotting four similar time series in which the heaviest 1–4 rainfall events from each year are excluded. Excluding the heavy events shifts the mean $\delta^{18}O$ higher and, in years like 2015 and 2018, can change annual means from anoma-

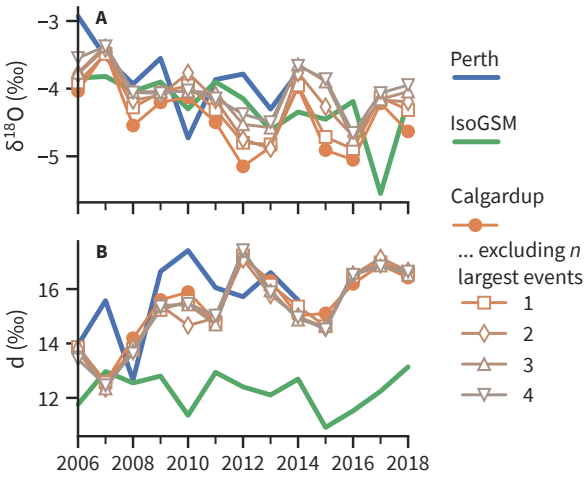

Figure 3. Annual precipitation-weighted mean **A** δ^{18}O and **B** d from Calgardup Cave and Perth. As well as showing the entire dataset, the annual mean values for Calgardup are also computed after incrementally leaving out the four largest daily rainfall accumulations, illustrating the sensitivity of interannual δ^{18}O variations, but not d variations, to a few events. Results from the IsoGSM isotope-enabled general circulation model are also shown.

lously low to high. As with any rainfall event, these heavy events will be sampled differently by the two monitoring sites (Good et al., 2014), so stochastic variability is a major contributor to the annual precipitation-weighted mean δ^{18}O. In contrast to δ^{18}O, the interannual variability in d is not as strongly affected by these intense rainfall events (Fig. 3b), so the annual-mean difference between Perth and Calgardup Cave time-series are not as sensitive to stochastic variability.

To examine the factors which drive these long-term changes, and the seasonal cycle, we analyze the conditions on each rainy day in the following sections.

4.4 Synoptic systems

Self organizing maps (SOMs) were used to classify synoptic regimes. We identified 35 synoptic types using MSLP fields from ERA-Interim, and each day was associated with one of types shown in Fig. 4. Supplementary interpretation is provided by the frontal density and 500 hPa height fields in Fig. S3, and Fig 5 summarizes several observations according to synoptic type.

Although the SOM is not derived directly from frontal information, the location of fronts is related to the surface pressure field and the synoptic types are therefore associated with front positions. The top two rows in the SOM are most strongly associated with the presence of rain-bearing cold fronts directly over SWWA, while the sequence around the outside edge of the SOM, A4$\cdots$A1$\cdots$E1, tracks the progress of cold fronts beginning offshore to the west and moving east across the region. This is a common occurrence, and appears as a path with high transition probabilities in Fig. 5a. Types in the top left are more representative of pre-frontal rainfall, while types in the top right are post-frontal.

Synoptic types away from the top rows are not as strongly associated with frontal rainfall (Fig. S3); although fronts are detected they are generally away from SWWA. Notably, the pressure pattern for classes A5, A6 resembles a trough, associated with mois-

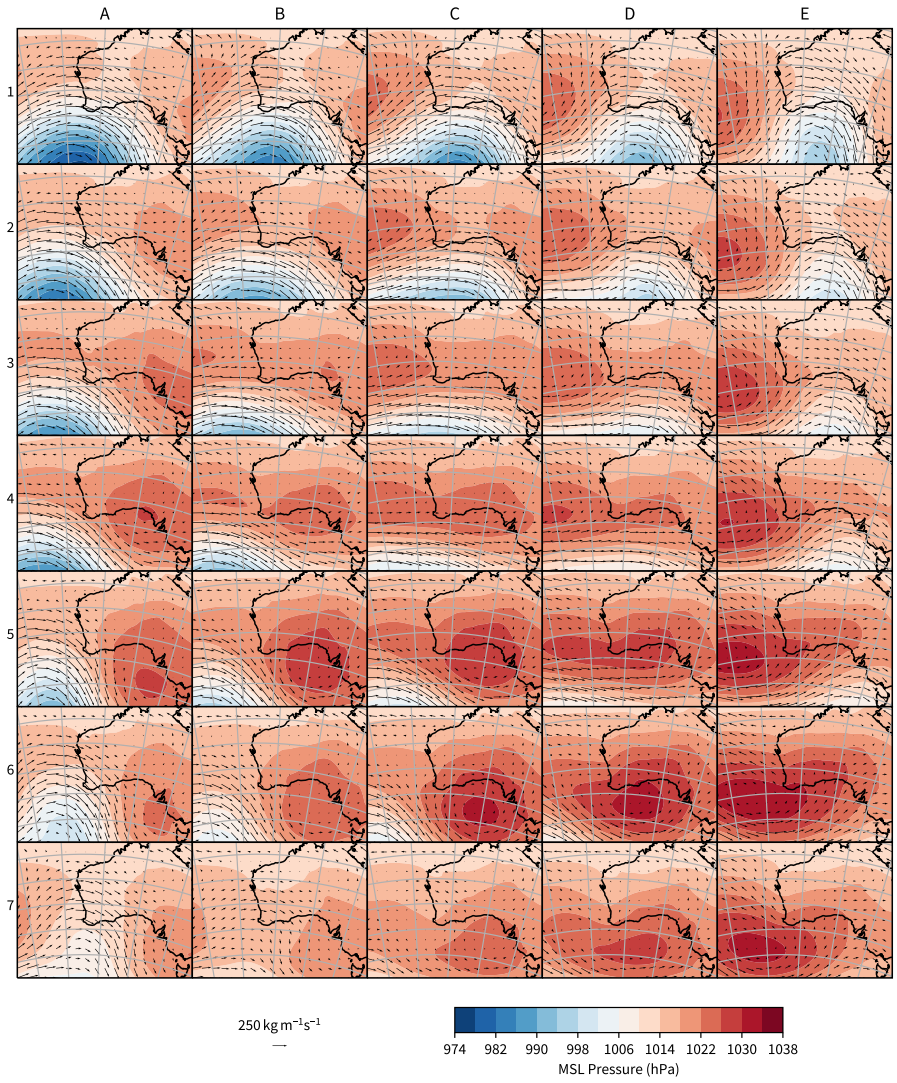

Figure 4. SOM–derived synoptic types, with mean-sea-level pressure and vertically-integrated water vapor transport.

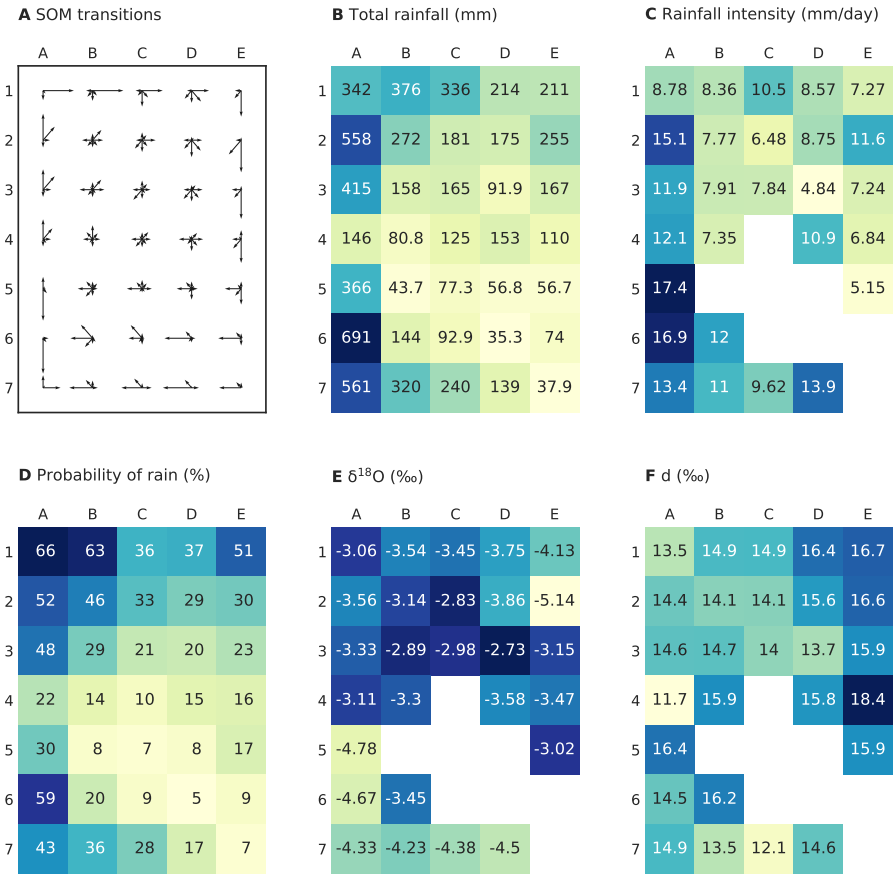

Figure 5. Rainfall, isotope, and SOM properties, 2006-18, by synoptic type. Panels show: **A** relative transition probability (longer arrows show more likely transitions); **B** accumulated precipitation; **C** rainfall intensity (mean rainfall per day); **D** probability of rainfall; **E** arithmetic mean δ^{18}O; **F** arithmetic mean deuterium excess, d. Colors are used to highlight patterns in the data, the number of days in each class ranges from 51 to 101, and cells with less than 10 observations are left blank in panels C, E, and F.

ture transport from the northwest, and A7 is a blend between a trough and cutoff low. These three classes, in general, are related to upper-tropospheric processes with fronts being detected too far to the west to be responsible for rainfall.

As shown in Fig. 5 synoptic types are a reasonable predictor of rainfall properties, several of which show a strong dependence on SOM classification. In particular, the wettest class (A1) has a rainfall probability of 66%, much higher than the driest class with 5% probability of rain (Fig. 5d). Rainfall intensity (Fig. 5c) is also sensitive to synoptic type, with column A showing the most intense rainfall, especially for classes A5 and A6. Although these non-frontal classes are associated with heavy rain, and A6 accounts for the highest total precipitation, frontal events are responsible for more rainfall overall as they occupy a larger number of classes. Based on manual classifications, Pook et al. (2012) also found that fronts were responsible for most winter rainfall.

Water isotopes show a weaker dependence on synoptic type than precipitation itself, but a relationship nevertheless exists (Fig. 5e and 5f). For δ^{18}O, frontal rainfall shows a trend towards lower δ^{18}O and higher d after the passage of the front, seen in the top row of these figures. Another pattern revealed by the SOM is that non-frontal rainfall is lower in δ^{18}O. Trends in d (Fig. 5f) are in the opposite direction, with the non-frontal class A5 having higher d than the frontal rainfall classes A1-A3.

These observations are consistent with other studies (Treble, Budd, et al., 2005; Barras & Simmonds, 2008) which have demonstrated, in the Australian region, that different types of synoptic systems can have distinct isotopic signatures, an effect which is replicated at sites elsewhere in the world (Baldini et al., 2010; Scholl et al., 2009). In particular, the anomalously low rainfall δ^{18}O observed from intense low pressure systems lying off the eastern coast of Australia (Crawford et al., 2017) is a similar finding to the low δ^{18}O and intense rainfall seen in classes A6 and A7.

The SOM analysis, while showing an association between synoptic types and isotopes, does not by itself identify the reasons behind the association. Furthermore, although there is a relatively large difference between frontal and non-frontal rainfall, δ^{18}O differing by 1–1.7‰, this difference is not large enough to explain the year-by-year variability (Fig. 3). Year-by-year changes can reach 1‰, meaning that rainfall would need to switch from almost exclusively frontal rainfall to non-frontal to explain the changes in annual mean δ^{18}O, and this is not something which is observed. In the next section, upstream conditions, diagnosed from dispersion modelling, are combined with site-based observations and synoptic types to gain more insight into the underlying processes.

4.5 Generalized additive model for δ^{18}O

Generalized additive models (GAMs) trained to predict daily rainfall δ^{18}O are shown in Fig. 6. These curves are the model's 'smooth terms', that is the smooth functions expressing the relationship between predictor variables and the response variable. Two models are shown, one with synoptic types (trained on data from the wet months, April–October) and another without synoptic types (trained on data from the entire year). In this figure, smooth terms are ordered according to how much they improve the daily mean-square error. This, and other metrics for judging the importance of terms, is shown in Fig. 7.

For predictions of daily δ^{18}O, the most important smooth terms in this model are: the locally-recorded rainfall intensity, P; the mean rainfall intensity along the backwards plume, $\overline{P}$; then source humidity, h_s relative to the sea surface temperature. Local rainfall intensity is the best predictor of daily δ^{18}O, the seasonal cycle, and year-to-year variability (Fig. 7), it follows a relationship which is close to $\delta^{18}\text{O} \propto \log(P)$. Adding the rainfall intensity, along the backwards plume, improves the model's fit to interannual variability, by almost as much as P, but does not affect its fit to the seasonal cycle. The third term, h_s is defined as the humidity in the evaporation region relative to the sea surface

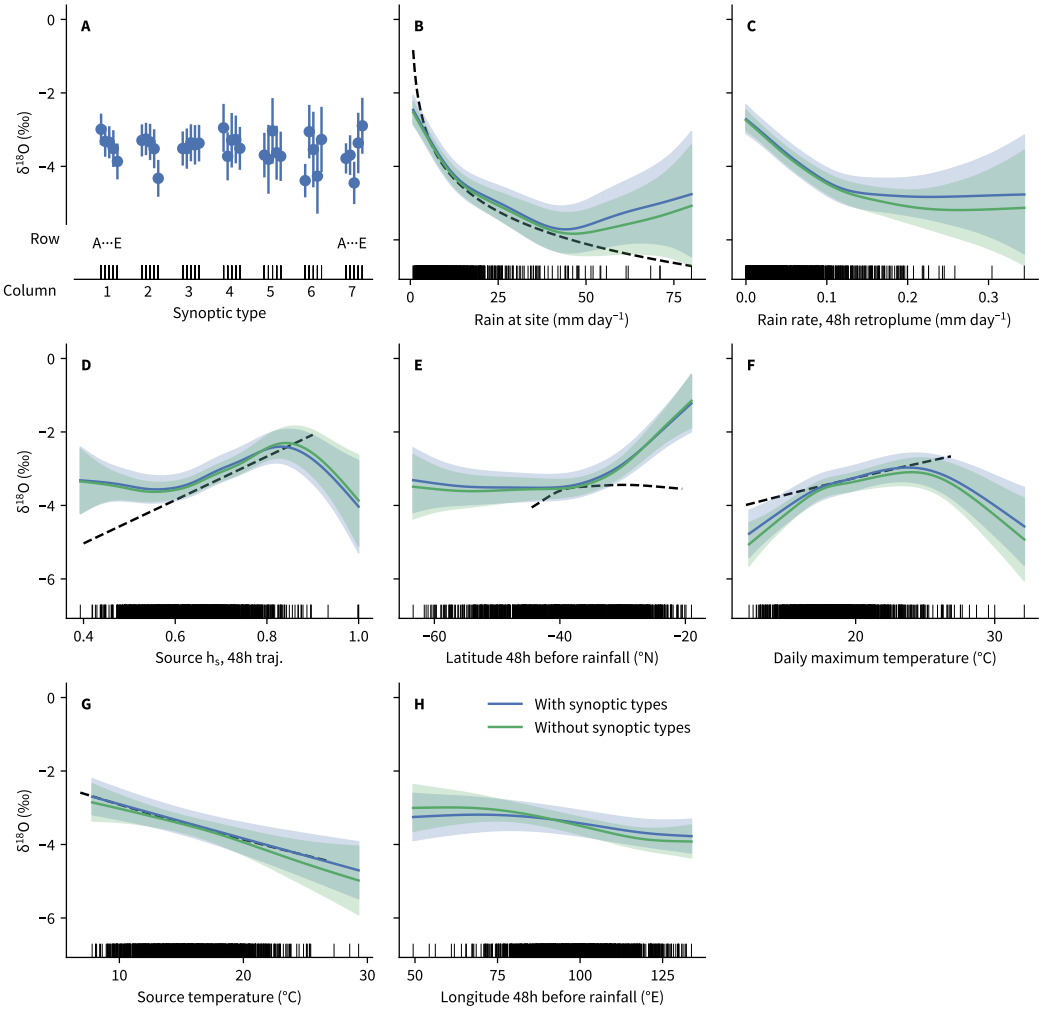

Figure 6. Categorical and smooth terms for a GAM predicting daily δ^{18}O. The categorical term is shown first, then smooth terms are shown in order of importance. Error bars or shading indicate the 95% confidence interval. Upward ticks on the x-axis of each plot indicate measurements and black dashed lines show other relationships: **B** $\log P$, an empirical fit; **D** kinetic fractionation (Merlivat & Jouzel, 1979; Benetti et al., 2014); **E** δ^{18}O latitudinal variation in Indian Ocean surface waters (LeGrande & Schmidt, 2006); **F**, **G** equilibrium fractionation factor dependence on temperature (Horita & Wesolowski, 1994).

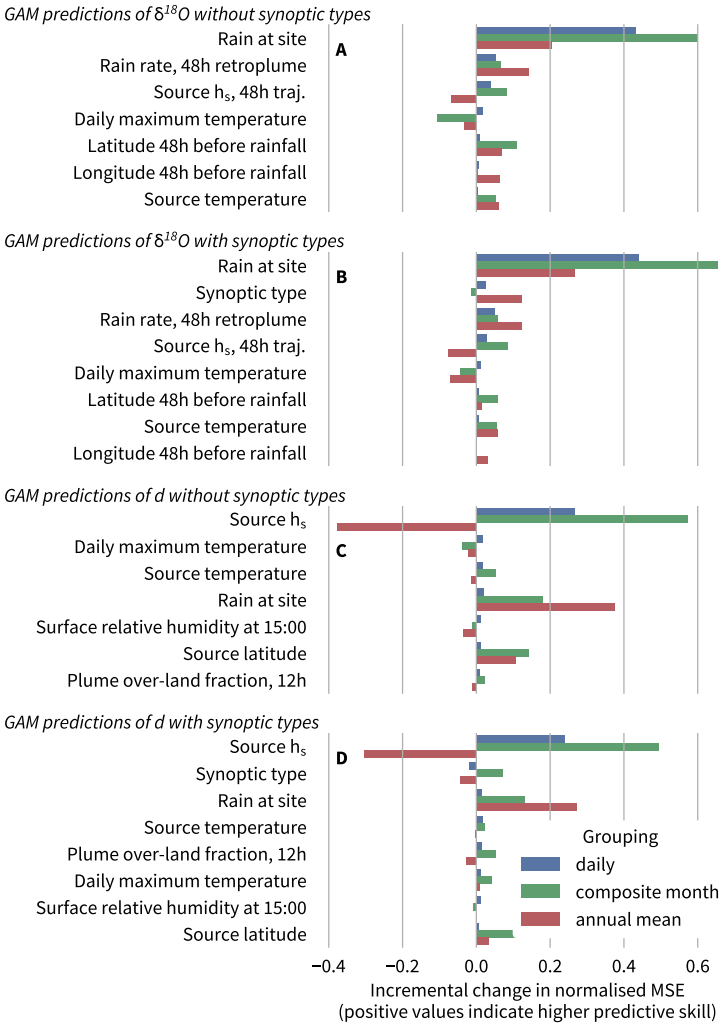

Figure 7. Prediction accuracy of GAM: **A** δ^{18}O predictions; **B** like A, but the additional 'synoptic type' predictor; **C** d predictions; **D** like C, but with synoptic types. Plots show the improvement in the cross-validated mean squared error (MSE) due to the addition of a predictor, compared with a simpler model which does not include that predictor. The simplest model, which begins the sequence, is a model which predicts the mean. MSE is normalized the by MSE of the 'constant value' model. In each category, three precipitation-weighted groupings are considered: 1. the ungrouped daily data; 2. monthly groups for a composite year; and 3. annual totals.

temperature. It is calculated from atmospheric properties within the lowest model level and weighted by evaporation rate. Source humidity is important for the δ^{18}O seasonal cycle, but not interannual variability. Even more than that, the inclusion of h_s increases the model error for the prediction of interannual variability.

Remaining terms do not make a major difference to the model's predictive ability at interannual scales (Fig. 7). Nevertheless, the starting latitude and longitude of the plume, along with the source temperature and backwards-plume overland fraction, are detected in the model as having an influence on δ^{18}O, and are discussed further in Sect. 5.

Despite being statistically-significant, including synoptic types as a predictor variable does not appreciably improve the overall model performance (Fig. 7), suggesting that synoptic types contain redundant information already contained in the smooth terms. The shape of the smooth terms is also insensitive to the presence of synoptic types, as seen in Fig. 6 where the GAM with synoptic types has similar smooth terms to the GAM without. There are also similarities in the patterns of Fig. 6a, which show the effect of synoptic type marginalized for the effect of other variables, to the patterns in Fig. 5e which showed the mean δ^{18}O in each synoptic type.

A comparison of GAM predicted δ^{18}O with observed timeseries is shown in Fig. 8a and 8b showing that the GAM successfully tracks δ^{18}O interannual variability and the seasonal cycle.

In summary, the combination of the GAM analysis with synoptic types supports the conclusions of earlier studies which have found that isotopic composition is related to synoptic types, but it also shows that there are underlying continuous variables which explain the isotopic composition, for this region, without needing to incorporate synoptic types. The continuous predictor variables have the advantages that they can be used in all months of the year and are less likely to cause over-fitting.

4.6 Generalized additive model for deuterium excess

Rainfall d differs from δ^{18}O both in terms of which predictors are important, and how well a GAM trained on daily data is able to predict interannual variability. As with δ^{18}O, a GAM was trained using daily data and then used to predict aggregate values over longer periods. This process was repeated with another GAM which included synoptic types.

The leading predictor of daily d is source humidity relative to saturation at the sea surface, h_s. This is followed by source temperature, T_s, site temperature (daily maximum temperature at Calgardup from a gridded data set; Jones et al., 2009), and rainfall intensity, P. Compared with h_s, the remaining terms only weakly improve the MSE at the daily scale (Fig. 7c), but only the inclusion of P is able to improve the annual-mean predictions, relative to a prediction of constant d.

The effect of adding synoptic types to the d model, which also means restricting the model to rainy months, is shown in Fig. 7d. Synoptic types, although statistically important according to the REML test, fail to improve the cross-validated MSE at the daily or interannual time scales. As with δ^{18}O, the information introduced to the model by the synoptic types is redundant, and reduces the cross-validated performance of the model, possibly because the large number of categories promotes over-fitting.

Of all the factors in this analysis, however, it is the source humidity which stands out. It is strongly linked to d at the daily scale, it is apparently the main driver of the observed seasonal cycle, but using it to predict interannual variability produces a very poor model—one which has a larger error than a model without h_s. When plotted alongside observations, the annual mean predictions of d (Fig. 8c) show that, in contrast to the case of δ^{18}O, the GAM is unable to follow the overall increasing trend in observed

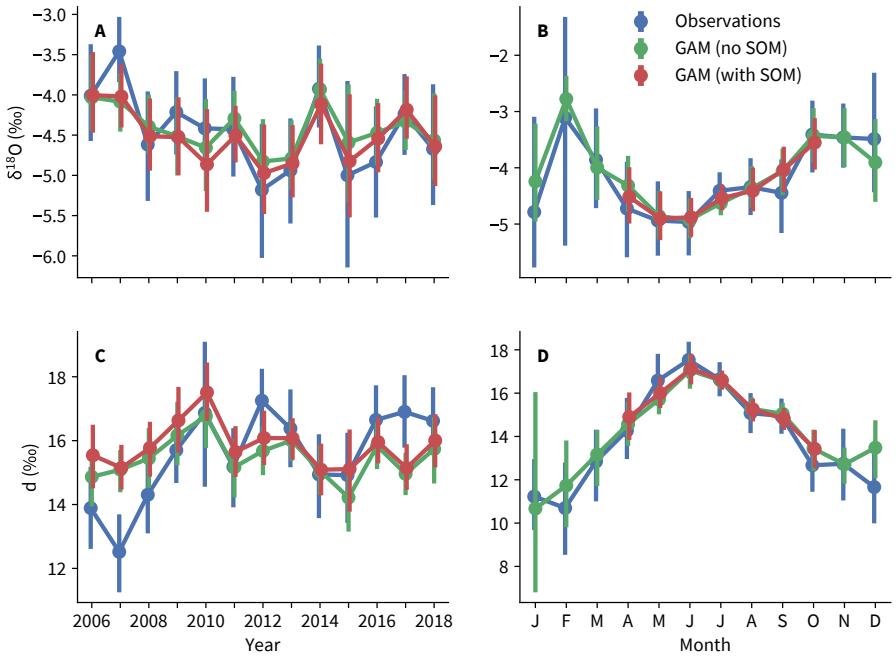

Figure 8. Precipitation-weighted GAM predictions versus observations: **A** annual δ^{18}O; **B** seasonal δ^{18}O; **C** annual d; and **D** seasonal d. Error bars show the 95% confidence interval from bootstrapping daily values.

rainfall d, even though it is largely successful at reproducing the seasonal cycle. The GAM predictions start above the observations and then are biased low by the end of the observation period (model residuals are shown more clearly in Fig. S4). An explanation for this apparent contradiction is that there is a missing term which is correlated with both h_s and d at the annual-mean timescale.

5 Discussion

5.1 Physical processes driving δ^{18}O

The predictor variables with the strongest link to rainfall δ^{18}O were rainfall intensity, observed at the site, P, and rainfall intensity modelled along the backwards plume, $\overline{P}$. These two predictors are only moderately correlated ($R = 0.30$, 95% CI $[0.25, 0.35]$) meaning that they are statistically different enough to represent different underlying processes, and yet they are conceptually similar enough to be driven by a single process. If both P and $\overline{P}$ are driven by the same process, this is likely a modified version of Rayleigh distillation (Eriksson, 1965).

During idealized Rayleigh distillation, an airmass is continually cooled, condensate forms in isotopic equilibrium with the vapor, this condensate is immediately removed from the system by rainout, and δ^{18}O of the remaining vapor can be expressed as function of the fraction of remaining moisture. But in the case of coastal rainfall, the system departs from the ideal in several ways. It is possible for moisture to be continually renewed by evaporation from the ocean (Moore et al., 2014), rainfall is not instantaneously removed allowing for partial evaporation of rainfall below the cloud base and recycling of moisture (Lee & Fung, 2008), and there is three-dimensional transport within synoptic systems which differs from the idealized model (Dütsch et al., 2016). Although the

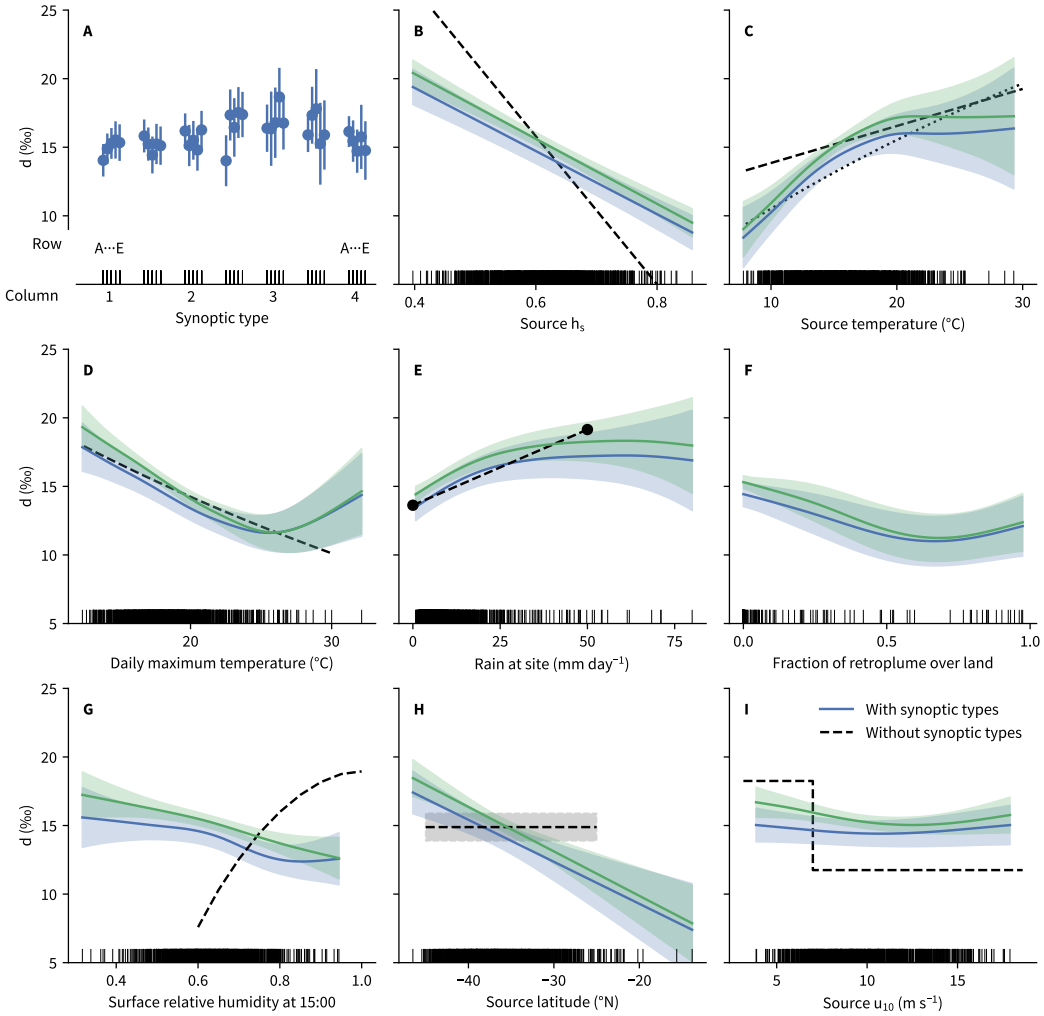

Figure 9. Smooth terms for GAM predicting daily d. Other relationships shown are: **B** empirical h_s relationship (Pfahl & Sodemann, 2014); **C** empirical T_s relationship (Bonne et al., 2019, dashes) and the effect of the temperature dependence of equilibrium fractionation factors (Horita et al., 2008, dots); **D** the effect of the temperature dependence of equilibrium fractionation factors applied to raindrops (Horita et al., 2008); **E** Xia and Winnick (2021) subcloud evaporation model with raindrop diameter at cloud base of 0.6 mm and 2.6 mm (surface temperature 18 °C, surface humidity 60%); **F** Xia and Winnick (2021) subcloud evaporation model humidity dependence (raindrop diameter 2.1 mm, surface temperature 18 °C); **H** indicative range of d observed in surface waters in the Atlantic Ocean (Bonne et al., 2019) and modelled in the Indian Ocean (Xu et al., 2012); **I** parameterisation from Merlivat and Jouzel (1979) at $h_s = 0.6$ (Benetti et al., 2014).

observations are not comprehensive enough to draw strong conclusions, they are consistent with the interpretation that P is correlated with past rainout, and hence Rayleigh-type processes, as well as being directly indicative of the importance of local post-condensation processes. The preferential rainout of heavy isotopes upstream of Calgardup Cave is closely related to $\overline{P}$, but this parameter is only available via model output and therefore has a large error. The fact that $\overline{P}$ has predictive power, almost as much as P at the interannual timescale despite being derived from model output, indicates that past rainfall is important.

Another way of considering the role of Rayleigh distillation is through the so-called continental effect (Winnick et al., 2014) which often appears as an important term driving δ^{18}O (Good et al., 2014, e.g.). Here, the fraction of the backwards plume over land, f_l (calculated after 3 h of travel), shows that airmasses which have spent more time over land have lower δ^{18}O, meaning that the trend in our results is consistent with isotopic depletion driven by rainout. On the whole, f_l is of only minor importance because the vast majority of trajectories do not pass over land before arriving at the rainfall site. Just over 90% of backwards plumes spend less than 0.1% of their time over land within 12 h of arrival. Because of the lack of overland trajectories in the data, it is unlikely that the GAM has been able to learn an accurate relationship, or be able to generalize well to inland sites, but the presence of a relationship between δ^{18}O and f_l indicates that rainout is able to drive depletion, making it likely that this process plays a role in the sensitivity of δ^{18}O to rainfall intensity.

This sensitivity to rainfall intensity acts on a timescale of individual storms. When aggregated from daily to monthly precipitation-weighted values, rainfall intensity has a stronger association with δ^{18}O than does total monthly precipitation. This is in agreement with Fischer and Treble (2008) who studied monthly δ^{18}O data from Perth and a short record of daily measurements from Cape Leeuwin. Also similar is that Fischer and Treble (2008) found a nonlinear relationship between precipitation and δ^{18}O, using $\delta^{18}\mathrm{O} \propto P^{\frac{1}{2}}$. In our data set, due to scatter, $\delta^{18}\mathrm{O} \propto P^{\frac{1}{2}}$ fits the data almost as well as $\delta^{18}\mathrm{O} \propto \log(P)$, and we plot the log form mainly out of preference because of its appearance in Rayleigh distillation and also the use of a log transformation when δ^{18}O is regressed against moisture residence time, τ. Aggarwal et al. (2012) found that $\delta^{18}\mathrm{O} \propto \tau = \log(Q/P)$ where Q is the total column water vapor and P is the long-term mean precipitation rate. In our data, variability in Q is small enough that $\log(P/P_0)$ is strongly correlated with τ so there is no advantage in changing variables to τ ($R = -0.94$, 95% CI $[-0.95, -0.93]$, Q from ERA-Interim).

Besides processes which happen during rainfall or in-transit, the properties of source moisture are also potential drivers of variability, and some of these are identified by the GAM. Source humidity, h_s affects δ^{18}O through kinetic fractionation. The relationship determined by the GAM is similar to the expression for kinetic fraction used by Benetti et al. (2014), as shown by the dashed line in Fig. 6d. In contrast, the relationship between latitude and δ^{18}O (Fig. 6e) does not follow the meridional variation in Indian Ocean surface water δ^{18}O (LeGrande & Schmidt, 2006). Fischer and Treble (2008) also reported a difference in δ^{18}O between airmasses travelling equatorward or poleward, but our results suggest that isotopic differences in the source waters are not responsible, meaning that perhaps it is the atmospheric δ^{18}O values at the beginning of the backwards plume which is important. This is plausible because of a strong and persistent meridional gradient in mean atmospheric δ^{18}O, with higher values towards the pole, which is a large driver of isotopic variability in idealized simulations (Dütsch et al., 2016). There are also several co-varying parameters which may obfuscate the direct effect of source water δ^{18}O; latitude is strongly correlated with the oceanic source temperature ($R = 0.91$ 95% CI $[0.9, 0.92]$), wind speed ($R = -0.61$ 95% CI $[-0.64, -0.57]$), and humidity ($R = 0.34$ 95% CI $[0.28, 0.39]$).

Also present in the GAM is the evaporation-weighted sea surface temperature, T_s. As indicated by the dashed line in Fig. 6g, this term is consistent with the temperature dependence of equilibrium fractionation of water vapor from the ocean surface (Majoube, 1971; Horita & Wesolowski, 1994). Fortuitously, and despite the presence of latitude in the model, the smooth term in the GAM matches the slope of the theoretical relationship very well.

5.2 Physical processes driving deuterium excess

The strongest predictor of daily d is the source humidity, h_s, although the relationship between d and h_s shows a lower slope (−30 ‰) than seen in studies of water vapor; the dashed line in Fig. 9b shows a typical slope of −54 ‰ (Pfahl & Sodemann, 2014). There are three potential explanations for this. First, this difference may be due to uncertainty in the h_s estimate. The standard deviation of the difference between FLEXPART and FLEXPART-WRF derived values, accounting for part of the uncertainty, is 0.04 which is large enough, based on tests with synthetic data, to reduce the slope of the line of best fit. Second, low humidity air during rainfall (small h) causes strong re-evaporation of rainfall (Risi et al., 2008). At this coastal site, h is moderately correlated with h_s (using modelled h, since h_s is model-derived, $R = 0.31$ 95% CI $[0.26, 0.36]$), so the two effects together act to reduce the observed slope between h_s and d. Third, the slope between d and h_s may be a genuine trait of the source region. Steen-Larsen et al. (2014) report a flatter slope for the $d \sim h_s$ relationship, with a slope of −42.6 ‰, and Aemisegger and Sjolte (2018) demonstrate the $d \sim h_s$ slope varies by region. Even accounting for regional variation however, −30 ‰ is sufficiently outside the range of other observations that a combination of the other factors too, h_s uncertainty or $h \sim h_s$ correlation, is likely to be important.

The effect of other sea surface parameters, temperature, T_s, and wind speed, u_{10}, have been investigated in the past and their importance is still debated. Uemura et al. (2008) reported a positive correlation between d and T_s in field measurements, in agreement with Bonne et al. (2019), whereas Pfahl and Sodemann (2014) argue that the T_s is of minor importance compared with h_s. Figure 9d shows that our data do indicate a positive correlation between d and T_s for $T_s < 20°\mathrm{C}$. The relationship between u_{10} and d is weak in the GAM (Fig. 9i), and arguably inconsistent with the Merlivat (1978a) relationship, in which kinetic fractionation, and hence d in evaporation, is lower at high wind speeds. In their parametrization, low wind speeds below about $7\,\mathrm{ms}^{-1}$ correspond to a smooth regime (and higher d) whereas high wind speeds are modelled by a rough regime (with lower d) (Merlivat & Jouzel, 1979). The u_{10} relationship here is too weak to match the parametrization and it weakens further when synoptic types are included. These findings are in agreement with other recent studies which have found that the Merlivat (1978a) parametrization is not directly applicable to field observations. Benetti et al. (2014) present data which lies between the rough and smooth regimes, Steen-Larsen et al. (2014) find no statistical difference in d in low versus high winds, and Bonne et al. (2019) also find there to be no effect on d from wind speed, with their data being best explained by the rough regime of the Merlivat and Jouzel (1979) model. Considered in the context of these other studies, then, the existence of a strong relationship between d and u_{10} seems unlikely.

Variability in d is also driven by the latitude of origin, which may either be linked to meridional variations in oceanic d or meridional variations in atmospheric d. Figure 9h shows that the change in d with latitude is much larger than observed and modelled variations in surface waters, meaning that atmospheric processes are more likely to be responsible.

Besides the conditions at the moisture source, a second driver of d is the post-condensation re-evaporation of droplets in the subcloud layer. The re-evaporation model of Xia and

Winnick (2021) is used for comparison with the GAM smooth terms, showing that the increase in d as a function of rainfall intensity is consistent with subcloud reevaporation. The model is a reasonable match to the smooth term when physically reasonable raindrop diameters of 0.6 and 2.6 mm are assumed for rain rates of 2 and 50 mm day^{-1} (Fig. 9e). In contrast, a calculation using the same model of the relationship between d and surface humidity (based on humidity at the surface measured at 1500 local time) does not even match the sign of the relationship between d and (Fig. 9g). This is likely to be the result of the predictor vairable, based on dewpoint temperature at 1500 local time, being a poor stand in for the humidity which is actually experienced during rainfall, which happens at an unknown time each day and over a relatively deep atmospheric layer between the cloud base and surface.

5.3 Generalizability of the model

As a test of the model's performance away from the observation site, predictions of δ^{18}O for Perth Airport were computed based on observed daily rainfall and FLEXPART backwards plumes terminating at Perth Airport on each rain day. Only δ^{18}O was analysed in detail, since the model was unable to reproduce interannual variations in d over the monitoring period at Calgardup Cave. GAM predictions were clipped to the range of observations to prevent extrapolation errors. In particular, on days with less than 2 mm of rainfall δ^{18}O was set to the same value as if 2 mm of rainfall was observed. This was necessary because many of the monthly accumulations included a nontrivial contribution from days with light rainfall.

When compared with monthly δ^{18}O observations, the GAM performed well during the wet months but had large errors during the dry months (Fig. S5). On some occasions, this was because of highly depleted rainfall sourced from the ocean off the northwest coast of Western Australia which had made a long transit over land. In general, the failure of the model to perform well during the summer months can be attributed to a lack of summer rainfall in the training data. The stronger influence of tropical processes in summer, on Perth rainfall, may also play a role.

When aggregated to annual data, the poor performance during dry months becomes inconsequential and the model generalizes well; performance in Perth shows a similar predictive skill to Calgardup Cave (Fig. S6). Furthermore, the GAM is able to reproduce the offset in mean δ^{18}O observed between Perth and Calgardup Cave. To reproduce the offset, the model needs to include rainfall intensity, rainfall along the backwards plume, source humidity, and source latitude. In particular, the difference in rainfall intensity between Perth and Calgardup Cave is only responsible for about 10% of the offset. The good performance of the model for the Perth observations makes it likely to be suitable for the interpretation of longer-term data from the coastal zone between Calgardup and Perth.

For deuterium excess, GAM predictions at Perth Airport show a similar error to the Calgardup Cave timeseries tending to have a low bias at the start of the observation period and a high bias towards the end.

5.4 Interpretation of water isotopes in paleoclimate studies

Based on data from the 13 year observing period, this study confirms that rainfall intensity is a primary driver of δ^{18}O in precipitation. The nonlinear relationship can be approximated as

$$\delta^{18}\mathrm{O} = \begin{cases} \alpha \log\left(P/P_0\right) + \beta, & P \geq 2\,\mathrm{mm\,day^{-1}} \\ -2.05‰, & P < 2\,\mathrm{mm\,day^{-1}}, \end{cases} \tag{3}$$

where $P_0 = 1\,\mathrm{mm\,day^{-1}}$, $\alpha = -2.85‰$, and $\beta = -1.19‰$. Importantly, years with more intense rainfall are not necessarily wetter overall. In our data, rainfall intensity (pre-

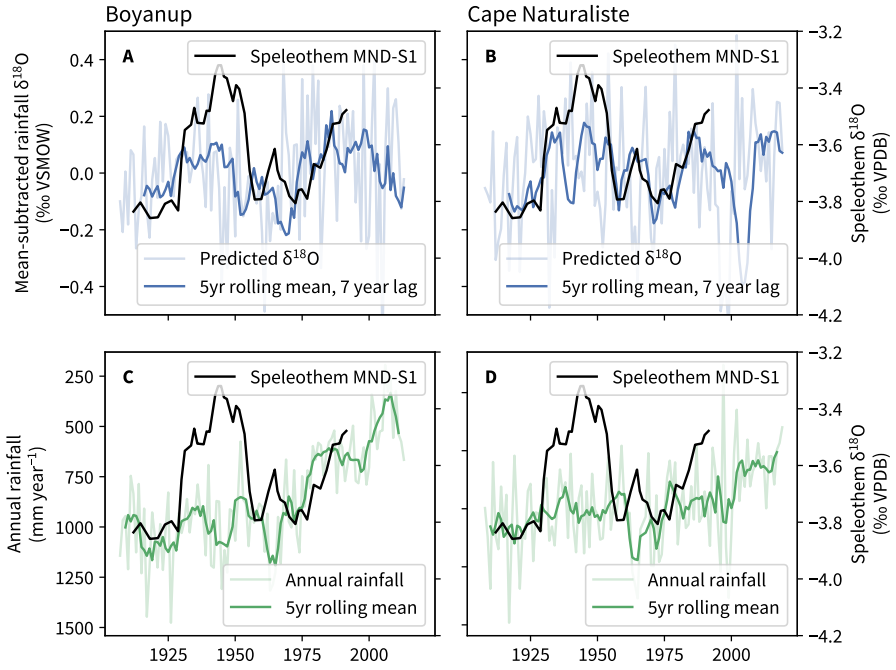

Figure 10. Speleothem MND-S1 from Moondyne Cave δ^{18}O (Treble, Chappell, et al., 2005) compared with **A** rainfall δ^{18}O inferred from Boyanup rainfall intensity, **B** Boyanup annual rainfall, **C** rainfall δ^{18}O inferred from Cape Naturaliste rainfall intensity, **D** Cape Naturaliste annual rainfall. A lag of 7 yr and smoothing with a 5 yr rolling mean has been applied to the inferred δ^{18}O timeseries for comparison with the lower resolution speleothem record which contains both analytical smoothing and attenuation due to karst flow paths. The y-axis for annual total rainfall is inverted to facilitate comparison with the speleothem d18O values.

cipitation weighted) has no significant correlation with annual rainfall ($R = 0.23$, 95% CI $[-0.37, 0.69]$).

In Fig. 10 we use 100 yr records of daily rainfall, along with Eq. (3), to hindcast the δ^{18}O timeseries at Boyanup and Cape Naturaliste and compare the δ^{18}O hindcast to a speleothem record from Moondyne Cave to the south (Treble, Chappell, et al., 2005). Although not the closest observations stations to the cave where the speleothem was collected, these are high quality stations (Lavery et al., 1997) in the Australian network (locations shown in Fig. 1) meaning they are sites with long observation records and have been screened for spurious trends. To generate the hindcast, we used only days marked in the record as single-day accumulations, and checked for a weekday dependence to avoid some known quality problems in the Australian record (Viney & Bates, 2004).

Although taking only the leading predictor into account, rainfall δ^{18}O inferred from the Boyanup record displays an intriguing similarity to the Moondyne Cave record, particularly the period of relatively higher speleothem δ^{18}O from 1930–55 and the upwards shift from the mid 1970s. There is also a marked similarity when rainfall intensity is taken from the Cape Naturaliste record, although with a divergence during the 1930–55 period. The disagreement which remains may be the result of nonlinear filtering caused by karst hydrological processes, which has only been accounted for crudely here by a combination of temporal averaging and introducing a time lag. Indeed the time lag, of 7 years, is longer than suggested by the field evidence which perhaps indicates that uncertain-

ties in the chronology play a role (Nagra et al., 2016, approx. 5 yr). Another complication is that changes in rainfall intensity, inferred from the instrumental record (Philip & Yu, 2020), are not spatially smooth and, as demonstrated in Fig. 3, even at the annual scale the δ^{18}O timeseries is sensitive to the heaviest events which would impact sites differently, even over short spatial scales.

Supporting the interpretation that rainfall intensity is key to determining δ^{18}O, on daily through to decadal timescales, the trends in annual rainfall accumulations show a weaker relationship with δ^{18}O (Fig. 10c and 10d). Post 1970, for the Boyanup hindcast, a drying trend coincides with a upwards shift in speleothem δ^{18}O. This may be a sign that the interaction between karst hydrology and δ^{18}O changes as the system dries out, but needs detailed investigation before making firm conclusions. A sustained change in intense rainfall events could be further amplified by karst flowpaths as intense rainfall events are likely to be more effective at initiating recharge of karst stores (Treble et al., 2013).

In the case of deuterium excess, the interpretation of multidecadal records in this region continues to be hampered by an incomplete understanding of governing processes. The strongest predictor on a daily scale, source humidity, makes model predictions worse on an interannual scale. Out of the predictors that we considered, rainfall intensity, measured at the collection site but not along the backwards plume, has the strongest effect on d. This driver is consistent with subcloud re-evaporation being important for driving interannual variability and, if this relationship holds over longer timeseries, it would drive an anticorrelation between d and δ^{18}O. Such an anticorrelation was indeed reported by Priestley et al. (2020), in a 35 ka groundwater record, which indicates that the observed relationships between δ^{18}O, d, and P may also be present over much longer time scales.

6 Conclusions

Water isotopes in precipitation were measured daily over thirteen years (2006–2018). Daily variability was found to be superimposed on weaker low-frequency trends which were driven by anomalous conditions in the first three years of monitoring: δ^{18}O decreases by $0.06\pm0.03\,‰\mathrm{yr}^{-1}$ and d increases by $0.24\pm0.07\,‰\mathrm{yr}^{-1}$, and trends tend to weaken or reverse in the second half of the monitoring period. The factors which drive δ^{18}O and d variability, on a range of timescales, were investigated using generalized additive models (GAMs), with upstream conditions diagnosed with backwards dispersion modelling and synoptic types determined using a statistical method. Although water isotopes demonstrated an association with synoptic types, these were ultimately not a strong driver of variability because, we infer, the synoptic types contained redundant information which was better expressed by continuous values derived from backwards-plume diagnostics.

Daily variability in δ^{18}O was driven primarily by rainfall intensity, both at the measurement site and upstream, in agreement with the main finding of Fischer and Treble (2008), which was based on a smaller data set. The δ^{18}O seasonal cycle was driven by seasonal changes in both rainfall intensity and source humidity. The relationship between rainfall intensity, at a daily scale, and δ^{18}O was robust. It applied at both the primary measurement station, Calgardup Cave, and to monthly accumulations from Perth Airport. The relationship also appears to be robust over longer time periods, as shown by projecting the $\delta^{18}\mathrm{O} \propto \log(P/P_0)$ relationship back through the ~ 100 yr period with rainfall observations and comparing to a speleothem record. Because of the relationship between rainfall intensity and δ^{18}O, annual accumulations of δ^{18}O are more sensitive to the heaviest rainfall events each year than annual accumulated rainfall is, which has implications both for the interpretation of δ^{18}O records and for how much nearby sites can be expected to agree with each other.

The behavior of d differed from δ^{18}O in several ways. On a daily scale, variability was driven primarily by h_s, although with a flatter slope than reported in studies of water vapor. The d seasonal cycle was also well explained mainly by h_s, with a weaker contribution from rainfall intensity. In contrast, year-to-year changes in h_s failed to explain the interannual signal in precipitation-weighted annual mean d, with the implication that multi-decadal, or longer, records of d should not be interpreted as a straightforward proxy record of h_s in this region. Furthermore, the link between rainfall intensity and d was too weak to drive the observed changes in d, meaning that the driver for low-frequency changes in d was not fully explained. Further investigation of d is warranted because d has other desirable properties; d is not as sensitive as δ^{18}O to extreme events, and there is a low-frequency signal in the observations at both Calgardup Caves and Perth which may be climate-related; meaning that the d signal carries information which supplements δ^{18}O.

7 Acknowledgements

The outcomes of this study contribute to ARC DP200100203 awarded to PCT. Water isotope measurements were undertaken at ANSTO and simulations were carried out at ANSTO's High Performance Computing facility. We gratefully acknowledge the assistance from the staff at Calgardup Caves (Department of Biodiversity, Conservations and Attractions) to conduct the cave monitoring. IsoGSM data which appears in this article was provided thanks to Kei Yoshimura. This paper has benefited from the insightful comments of three anonymous reviewers whose contribution is appreciated. We also acknowledge the open-source software used in this project, especially: R; mgcv; Python; Pandas; SOM-PAK; and QGIS.

8 Data availability

The water isotope measurements from Calgardup Cave are available from the IAEA Water Isotope System for data analysis, visualization and Electronic Retrieval, https://nucleus.iaea.org/wiser/ using station code 9564101. Water isotopes measured at Perth Airport are available from https://openscience.ansto.gov.au/collection/881. The models used in this study are available for download, FLEXPART and FLEXPART-WRF from http://www.flexpart.eu/ and WRF from http://www.mmm.ucar.edu/wrf/users/. Reanalysis data are archived by the European Centre for Medium Range Weather Forecasting (ERA-Interim, https://www.ecmwf.int/en/foreca datasets/era-interim) and the National Oceanic and Atmospheric Administration (CFSR, https://www.ncdc.noaa.gov/data-access/model-data/model-datasets/climate-forecast-system-version2-cfsv2). Weather station and gridded climate data are available from the Australian Bureau of Meteorology, http://www.bom.gov.au.

References

Aemisegger, F., & Sjolte, J. (2018). A Climatology of Strong Large-Scale Ocean Evaporation Events. Part II: Relevance for the Deuterium Excess Signature of the Evaporation Flux. *J. Climate*, *31*(18), 7313–7336. doi: 10.1175/JCLI-D-17-0592.1

Aggarwal, P. K., Alduchov, O. A., Froehlich, K. O., Araguas-Araguas, L. J., Sturchio, N. C., & Kurita, N. (2012). Stable isotopes in global precipitation: A unified interpretation based on atmospheric moisture residence time. *Geophys. Res. Lett.*, *39*(11). doi: 10.1029/2012GL051937

Aggarwal, P. K., Romatschke, U., Araguas-Araguas, L., Belachew, D., Longstaffe, F. J., Berg, P., ... Funk, A. (2016). Proportions of convective and stratiform precipitation revealed in water isotope ratios. *Nature Geosci*, *9*(8), 624–629. doi: 10.1038/ngeo2739

Baldini, L. M., McDermott, F., Baldini, J. U. L., Fischer, M. J., & Möllhoff, M. (2010). An investigation of the controls on Irish precipitation δ18O values on monthly and event timescales. *Clim Dyn*, *35*(6), 977–993. doi: 10.1007/s00382-010-0774-6

Barras, V., & Simmonds, I. (2008). Synoptic controls upon δ^{18}O in southern Tasmanian precipitation. *Geophys. Res. Lett.*, *35*(2). doi: 10.1029/2007GL031835

Barras, V., & Simmonds, I. (2009). Observation and modeling of stable water isotopes as diagnostics of rainfall dynamics over southeastern Australia. *J. Geophys. Res. Atmospheres*, *114*(D23), D23308. doi: 10.1029/2009JD012132

Bates, B. C., Hope, P., Ryan, B., Smith, I., & Charles, S. (2008). Key findings from the Indian Ocean Climate Initiative and their impact on policy development in Australia. *Clim. Change*, *89*(3), 339–354.

Benetti, M., Reverdin, G., Pierre, C., Merlivat, L., Risi, C., Steen-Larsen, H. C., & Vimeux, F. (2014). Deuterium excess in marine water vapor: Dependency on relative humidity and surface wind speed during evaporation. *J. Geophys. Res. Atmos.*, *119*(2), 584–593. doi: 10.1002/2013JD020535

Bonne, J.-L., Behrens, M., Meyer, H., Kipfstuhl, S., Rabe, B., Schönicke, L., ... Werner, M. (2019). Resolving the controls of water vapour isotopes in the Atlantic sector. *Nat Commun*, *10*(1), 1–10. doi: 10.1038/s41467-019-09242-6

Brioude, J., Arnold, D., Stohl, A., Cassiani, M., Morton, D., Seibert, P., ... Wotawa, G. (2013). The Lagrangian particle dispersion model FLEXPART-WRF version 3.1. *Geosci. Model Dev.*, *6*(6), 1889–1904. doi: 10.5194/gmd-6-1889-2013

Brook, E. J., & Buizert, C. (2018). Antarctic and global climate history viewed from ice cores. *Nature*, *558*(7709), 200. doi: 10.1038/s41586-018-0172-5

Cai, W., Shi, G., & Li, Y. (2005). Multidecadal fluctuations of winter rainfall over southwest Western Australia simulated in the CSIRO Mark 3 coupled model. *Geophys. Res. Lett.*, *32*(12). doi: 10.1029/2005GL022712

Chen, Z., Auler, A. S., Bakalowicz, M., Drew, D., Griger, F., Hartmann, J., ... Goldscheider, N. (2017). The World Karst Aquifer Mapping project: Concept, mapping procedure and map of Europe. *Hydrogeol J*, *25*(3), 771–785. doi: 10.1007/s10040-016-1519-3

Comas-Bru, L., Rehfeld, K., Roesch, C., Amirnezhad-Mozhdehi, S., Harrison, S. P., Atsawawaranunt, K., ... SISAL Working Group members (2020). SISALv2: A comprehensive speleothem isotope database with multiple age–depth models. *Earth Syst. Sci. Data*, *12*(4), 2579–2606. doi: 10.5194/essd-12-2579-2020

Craig, H. (1961). Isotopic Variations in Meteoric Waters. *Science*, *133*(3465), 1702–1703. doi: 10.1126/science.133.3465.1702

Crawford, J., Hollins, S. E., Meredith, K. T., & Hughes, C. E. (2017). Precipitation stable isotope variability and subcloud evaporation processes in a semi-arid region. *Hydrol. Process.*, *31*(1), 20–34. doi: 10.1002/hyp.10885

Crawford, J., Hughes, C. E., & Lykoudis, S. (2014). Alternative least squares methods for determining the meteoric water line, demonstrated using GNIP data. *Journal of Hydrology*, *519*, 2331–2340. doi: 10.1016/j.jhydrol.2014.10.033

Dansgaard, W. (1964). Stable isotopes in precipitation. *Tellus*, *16*(4), 436–468. doi: 10.3402/tellusa.v16i4.8993

Dee, D. P., Uppala, S. M., Simmons, A. J., Berrisford, P., Poli, P., Kobayashi, S., ... Vitart, F. (2011). The ERA-Interim reanalysis: Configuration and performance of the data assimilation system. *Q.J.R. Meteorol. Soc.*, *137*(656), 553–597. doi: 10.1002/qj.828

Deininger, M., Werner, M., & McDermott, F. (2016). North Atlantic Oscillation controls on oxygen and hydrogen isotope gradients in winter precipitation across Europe; implications for palaeoclimate studies. *Clim. Past*, *12*(11), 2127–2143. doi: 10.5194/cp-12-2127-2016

Dey, R., Lewis, S. C., Arblaster, J. M., & Abram, N. J. (2019). A review of past and

projected changes in Australia's rainfall. *Wiley Interdiscip. Rev. Clim. Change*, *10*(3), e577. doi: 10.1002/wcc.577

Dütsch, M., Pfahl, S., & Sodemann, H. (2017). The impact of nonequilibrium and equilibrium fractionation on two different deuterium excess definitions. *J. Geophys. Res. Atmospheres*, *122*(23), 12,732–12,746. doi: 10.1002/2017JD027085

Dütsch, M., Pfahl, S., & Wernli, H. (2016). Drivers of δ^2H variations in an idealized extratropical cyclone. *Geophys. Res. Lett.*, *43*(10), 5401–5408. doi: 10.1002/2016GL068600

England, M. H., Ummenhofer, C. C., & Santoso, A. (2006). Interannual rainfall extremes over southwest Western Australia linked to Indian Ocean climate variability. *J. Climate*, *19*(10), 1948–1969. doi: 10.1175/JCLI3700.1

Eriksson, E. (1965). Deuterium and oxygen-18 in precipitation and other natural waters Some theoretical considerations1. *Tellus*, *17*(4), 498–512. doi: 10.1111/j.2153-3490.1965.tb00212.x

Farlin, J., Lai, C.-T., & Yoshimura, K. (2013). Influence of synoptic weather events on the isotopic composition of atmospheric moisture in a coastal city of the western United States. *Water Resour. Res.*, *49*(6), 3685–3696. doi: 10.1002/wrcr.20305

Fischer, M. J., & Treble, P. C. (2008). Calibrating climate-δ^{18}O regression models for the interpretation of high-resolution speleothem δ^{18}O time series. *J. Geophys. Res.-Atmospheres*, *113*(D17). doi: 10.1029/2007JD009694

Fohlmeister, J., Schröder-Ritzrau, A., Scholz, D., Spötl, C., Riechelmann, D. F. C., Mudelsee, M., ... Mangini, A. (2012). Bunker Cave stalagmites: An archive for central European Holocene climate variability. *Clim. Past*, *8*(5), 1751–1764. doi: 10.5194/cp-8-1751-2012

Foley, G. R., & Hanstrum, B. N. (1994). The capture of tropical cyclones by cold fronts off the west coast of Australia. *Wea. Forecasting*, *9*(4), 577–592. doi: 10.1175/1520-0434(1994)009⟨0577:TCOTCB⟩2.0.CO;2

Forster, C., Stohl, A., & Seibert, P. (2007). Parameterization of convective transport in a Lagrangian particle dispersion model and its evaluation. *J. Appl. Meteorol. Climatol.*, *46*(4), 403–422. doi: 10.1175/JAM2470.1

Frederiksen, J. S., & Frederiksen, C. S. (2007). Interdecadal changes in southern hemisphere winter storm track modes. *Tellus Dyn. Meteorol. Oceanogr.*, *59*(5), 599–617. doi: 10.1111/j.1600-0870.2007.00264.x

Geoscience Australia. (2012). *Surface Geology of Australia, 1:1 000 000 scale, 2012 edition.* http://data.bioregionalassessments.gov.au/dataset/8284767e-b5b1-4d8b-b8e6-b334fa972611.

Geoscience Australia, & Australian Stratigraphy Commission. (2017). *Australian Stratigraphic Units Database.* http://www.ga.gov.au/products-services/data-applications/reference-databases/stratigraphic-units.html.

Good, S. P., Mallia, D. V., Lin, J. C., & Bowen, G. J. (2014). Stable isotope analysis of precipitation samples obtained via crowdsourcing reveals the spatiotemporal evolution of Superstorm Sandy. *PLoS ONE*, *9*(3), e91117. doi: 10.1371/journal.pone.0091117

Guan, H., Zhang, X., Skrzypek, G., Sun, Z., & Xu, X. (2013). Deuterium excess variations of rainfall events in a coastal area of South Australia and its relationship with synoptic weather systems and atmospheric moisture sources. *J. Geophys. Res. Atmospheres*, *118*(2), 1123–1138. doi: 10.1002/jgrd.50137

Haylock, M., & Nicholls, N. (2000). Trends in extreme rainfall indices for an updated high quality data set for Australia, 1910–1998. *Int. J. Climatol.*, *20*(13), 1533–1541. doi: 10.1002/1097-0088(20001115)20:13⟨1533::AID-JOC586⟩3.0.CO;2-J

Hollins, S. E., Hughes, C. E., Crawford, J., Cendón, D. I., & Meredith, K. T. (2018). Rainfall isotope variations over the Australian continent – Implications for hydrology and isoscape applications. *Science of The Total Environment*, *645*,

630–645. doi: 10.1016/j.scitotenv.2018.07.082

Hope, P., Drosdowsky, W., & Nicholls, N. (2006). Shifts in the synoptic systems influencing southwest Western Australia. *Clim. Dyn.*, *26*(7-8), 751–764. doi: 10.1007/s00382-006-0115-y

Hope, P., Keay, K., Pook, M., Catto, J., Simmonds, I., Mills, G., ... Berry, G. (2014). A comparison of automated methods of front recognition for climate studies: A case study in southwest Western Australia. *Mon. Wea. Rev.*, *142*(1), 343–363. doi: 10.1175/MWR-D-12-00252.1

Horita, J., Rozanski, K., & Cohen, S. (2008). Isotope effects in the evaporation of water: A status report of the Craig-Gordon model. *Isotopes Environ Health Stud*, *44*(1), 23–49. doi: 10.1080/10256010801887174

Horita, J., & Wesolowski, D. J. (1994). Liquid-vapor fractionation of oxygen and hydrogen isotopes of water from the freezing to the critical temperature. *Geochimica et Cosmochimica Acta*, *58*(16), 3425–3437.

Hughes, C. E., & Crawford, J. (2012). A new precipitation weighted method for determining the meteoric water line for hydrological applications demonstrated using Australian and global GNIP data. *Journal of Hydrology*, *464–465*, 344–351. doi: 10.1016/j.jhydrol.2012.07.029

IAEA. (2006). *Reference sheet for international measurement standards* (Tech. Rep.). Vienna, Austria.

Jones, D., Wang, W., & Fawcett, R. (2009). High-quality spatial climate data-sets for Australia. *AMOJ*, *58*(04), 233–248. doi: 10.22499/2.5804.003

Jouzel, J., Masson-Delmotte, V., Cattani, O., Dreyfus, G., Falourd, S., Hoffmann, G., ... Wolff, E. W. (2007). Orbital and Millennial Antarctic Climate Variability over the Past 800,000 Years. *Science*, *317*(5839), 793–796. doi: 10.1126/science.1141038

Kohonen, T., Hynninen, J., Kangas, J., & Laaksonen, J. (1996). *SOM_PAK: The Self-Organizing Map Program Package.* https://www.semanticscholar.org/paper/SOM_PAK%3A-The-Self-Organizing-Map-Program-Package-Kohonen-Hynninen/7bd2bb8319a75d9140fd4c30431c7283a6b25710.

Krklec, K., & Domínguez-Villar, D. (2014). Quantification of the impact of moisture source regions on the oxygen isotope composition of precipitation over Eagle Cave, central Spain. *Geochimica et Cosmochimica Acta*, *134*, 39–54. doi: 10.1016/j.gca.2014.03.011

Lachniet, M. S. (2009). Climatic and environmental controls on speleothem oxygen-isotope values. *Quaternary Science Reviews*, *28*(5–6), 412–432. doi: 10.1016/j.quascirev.2008.10.021

Lavery, B., Joung, G., & Nicholls, N. (1997). An extended high-quality historical rainfall dataset for Australia. *Australian Meteorological Magazine*, *46*(1), 27–38.

Lee, J.-E., & Fung, I. (2008). "Amount effect" of water isotopes and quantitative analysis of post-condensation processes. *Hydrol. Process.*, *22*(1), 1–8. doi: 10.1002/hyp.6637

Lee, J.-E., Fung, I., DePaolo, D. J., & Henning, C. C. (2007). Analysis of the global distribution of water isotopes using the NCAR atmospheric general circulation model. *J. Geophys. Res.*, *112*(D16), D16306. doi: 10.1029/2006JD007657

LeGrande, A. N., & Schmidt, G. A. (2006). Global gridded data set of the oxygen isotopic composition in seawater. *Geophys. Res. Lett.*, *33*(12). doi: 10.1029/2006GL026011

Liu, J., Fu, G., Song, X., Charles, S. P., Zhang, Y., Han, D., & Wang, S. (2010). Stable isotopic compositions in Australian precipitation. *J. Geophys. Res. Atmospheres*, *115*(D23), D23307. doi: 10.1029/2010JD014403

Lorrey, A., Williams, P., Salinger, J., Martin, T., Palmer, J., Fowler, A., ... Neil, H. (2008). Speleothem stable isotope records interpreted within a multi-proxy

framework and implications for New Zealand palaeoclimate reconstruction. *Quaternary International*, *187*(1), 52–75. doi: 10.1016/j.quaint.2007.09.039

Lucas, C., Rudeva, I., Nguyen, H., Boschat, G., & Hope, P. (2021). Variability and changes to the mean meridional circulation in isentropic coordinates. *Clim Dyn*. doi: 10.1007/s00382-021-05903-9

Lykoudis, S. P., Kostopoulou, E., & Argiriou, A. A. (2010). Stable isotopic signature of precipitation under various synoptic classifications. *Physics and Chemistry of the Earth, Parts A/B/C*, *35*(9), 530–535. doi: 10.1016/j.pce.2009.09.002

Majoube, M. (1971). Fractionnement en oxygene-18 et en deuterium entre l'eau et sa vapeur. *J. Chim. phys*, *68*(10), 1423–1436.

McCabe-Glynn, S., Johnson, K. R., Strong, C., Berkelhammer, M., Sinha, A., Cheng, H., & Edwards, R. L. (2013). Variable North Pacific influence on drought in southwestern North America since AD 854. *Nat. Geosci.*, *6*(8), 617–621. doi: 10.1038/ngeo1862

Merlivat, L. (1978a). The dependence of bulk evaporation coefficients on air-water interfacial conditions as determined by the isotopic method. *J. Geophys. Res.*, *83*(C6), 2977–2980. doi: 10.1029/JC083iC06p02977

Merlivat, L. (1978b). Molecular diffusivities of $H_2{}^{16}O$, $HD^{16}O$, and $H_2{}^{18}O$ in gases. *The Journal of Chemical Physics*, *69*(6), 2864–2871. doi: 10.1063/1.436884

Merlivat, L., & Jouzel, J. (1979). Global climatic interpretation of the deuterium-oxygen 18 relationship for precipitation. *J. Geophys. Res.*, *84*(C8), 5029–5033. doi: 10.1029/JC084iC08p05029

Moerman, J. W., Cobb, K. M., Adkins, J. F., Sodemann, H., Clark, B., & Tuen, A. A. (2013). Diurnal to interannual rainfall $\delta^{18}O$ variations in northern Borneo driven by regional hydrology. *Earth and Planetary Science Letters*, *369–370*, 108–119. doi: 10.1016/j.epsl.2013.03.014

Moore, M., Kuang, Z., & Blossey, P. N. (2014). A moisture budget perspective of the amount effect. *Geophys. Res. Lett.*, *41*(4), 1329–1335. doi: 10.1002/2013GL058302

Nagra, G., Treble, P. C., Andersen, M. S., Fairchild, I. J., Coleborn, K., & Baker, A. (2016). A post-wildfire response in cave dripwater chemistry. *Hydrol. Earth Syst. Sci.*, *20*(7), 2745–2758. doi: 10.5194/hess-20-2745-2016

Noone, D., & Simmonds, I. (2002). Associations between $\delta^{18}O$ of Water and Climate Parameters in a Simulation of Atmospheric Circulation for 1979–95. *J. Climate*, *15*(22), 3150–3169. doi: 10.1175/1520-0442(2002)015⟨3150:ABOOWA⟩2.0.CO;2

Okazaki, A., Satoh, Y., Tremoy, G., Vimeux, F., Scheepmaker, R., & Yoshimura, K. (2015). Interannual variability of isotopic composition in water vapor over western Africa and its relationship to ENSO. *Atmos. Chem. Phys.*, *15*(6), 3193–3204. doi: 10.5194/acp-15-3193-2015

Orland, I. J., Bar-Matthews, M., Kita, N. T., Ayalon, A., Matthews, A., & Valley, J. W. (2009). Climate deterioration in the Eastern Mediterranean as revealed by ion microprobe analysis of a speleothem that grew from 2.2 to 0.9 ka in Soreq Cave, Israel. *Quat. Res.*, *71*(1), 27–35. doi: 10.1016/j.yqres.2008.08.005

Paget, M. J. (2008). *MODIS Land data sets for the Australian region* (Tech. Rep.). Canberra: CSIRO Marine and Atmospheric Research.

Pepler, A. S., Dowdy, A. J., van Rensch, P., Rudeva, I., Catto, J. L., & Hope, P. (2020). The contributions of fronts, lows and thunderstorms to southern Australian rainfall. *Clim Dyn*, *55*(5), 1489–1505. doi: 10.1007/s00382-020-05338-8

Pfahl, S., & Sodemann, H. (2014). What controls deuterium excess in global precipitation? *Clim. Past*, *10*(2), 771–781. doi: 10.5194/cp-10-771-2014

Pfahl, S., & Wernli, H. (2008). Air parcel trajectory analysis of stable isotopes in water vapor in the eastern Mediterranean. *J. Geophys. Res. Atmospheres*, *113*(D20), D20104. doi: 10.1029/2008JD009839

Pfahl, S., & Wernli, H. (2009). Lagrangian simulations of stable isotopes in water vapor: An evaluation of nonequilibrium fractionation in the Craig-Gordon model. *J. Geophys. Res.*, *114*(D20), D20108.

Philip, P., & Yu, B. (2020). Interannual variations in rainfall of different intensities in South West of Western Australia. *Int. J. Climatol.*, *40*(6), 3052–3071. doi: 10.1002/joc.6382

Philipp, A., Beck, C., Huth, R., & Jacobeit, J. (2016). Development and comparison of circulation type classifications using the COST 733 dataset and software. *Int. J. Climatol.*, *36*(7), 2673–2691. doi: 10.1002/joc.3920

Pook, M. J., Risbey, J. S., & McIntosh, P. C. (2012). The synoptic climatology of cool-season rainfall in the central wheatbelt of Western Australia. *Mon. Wea. Rev.*, *140*(1), 28–43. doi: 10.1175/MWR-D-11-00048.1

Power, S., Sadler, B., & Nicholls, N. (2005). The influence of climate science on water management in Western Australia: Lessons for climate scientists. *Bull. Amer. Meteor. Soc.*, *86*(6), 839–844. doi: 10.1175/BAMS-86-6-839

Priestley, S. C., Meredith, K. T., Treble, P. C., Cendón, D. I., Griffiths, A. D., Hollins, S. E., ... Pigois, J.-P. (2020). A 35 ka record of groundwater recharge in south-west Australia using stable water isotopes. *Sci. Total Environ.*, *717*, 135105. doi: 10.1016/j.scitotenv.2019.135105

R Core Team. (2014). *R: A language and environment for statistical computing* (Tech. Rep.). Vienna, Austria.

Raut, B. A., Jakob, C., & Reeder, M. J. (2014). Rainfall changes over southwestern Australia and their relationship to the Southern Annular Mode and ENSO. *J. Climate*, *27*(15), 5801–5814. doi: 10.1175/JCLI-D-13-00773.1

Raut, B. A., Reeder, M. J., & Jakob, C. (2016). Trends in CMIP5 Rainfall Patterns over Southwestern Australia. *J. Climate*, *30*(5), 1779–1788. doi: 10.1175/JCLI-D-16-0584.1

Risi, C., Bony, S., & Vimeux, F. (2008). Influence of convective processes on the isotopic composition (δ^{18}O and δD) of precipitation and water vapor in the tropics: 2. Physical interpretation of the amount effect. *J. Geophys. Res.*, *113*(D19), D19306. doi: 10.1029/2008JD009943

Risi, C., Bony, S., Vimeux, F., & Jouzel, J. (2010). Water-stable isotopes in the LMDZ4 general circulation model: Model evaluation for present-day and past climates and applications to climatic interpretations of tropical isotopic records. *J. Geophys. Res. Atmospheres*, *115*(D12), D12118. doi: 10.1029/2009JD013255

Risi, C., Noone, D., Worden, J., Frankenberg, C., Stiller, G., Kiefer, M., ... Sturm, C. (2012). Process-evaluation of tropospheric humidity simulated by general circulation models using water vapor isotopologues: 1. Comparison between models and observations. *J. Geophys. Res. Atmospheres*, *117*(D5). doi: 10.1029/2011JD016621

Rudeva, I., Simmonds, I., Crock, D., & Boschat, G. (2019). Midlatitude fronts and variability in the Southern Hemisphere tropical width. *J. Clim.*, *32*(23), 8243–8260. doi: 10.1175/JCLI-D-18-0782.1

Saha, S., Moorthi, S., Pan, H.-L., Wu, X., Wang, J., Nadiga, S., ... Goldberg, M. (2010). The NCEP Climate Forecast System Reanalysis. *Bull. Amer. Meteor. Soc.*, *91*(8), 1015–1058. doi: 10.1175/2010BAMS3001.1

Schemm, S., Rudeva, I., & Simmonds, I. (2015). Extratropical fronts in the lower troposphere–global perspectives obtained from two automated methods. *Q. J. R. Meteorol. Soc.*, *141*(690), 1686–1698. doi: 10.1002/qj.2471

Schlosser, E., Dittmann, A., Stenni, B., Powers, J. G., Manning, K. W., Masson-Delmotte, V., ... Scarchilli, C. (2017). The influence of the synoptic regime on stable water isotopes in precipitation at Dome C, East Antarctica. *The Cryosphere*, *11*(5), 2345–2361. doi: 10.5194/tc-11-2345-2017

Schmidt, G. A., LeGrande, A. N., & Hoffmann, G. (2007). Water isotope expres-

sions of intrinsic and forced variability in a coupled ocean-atmosphere model. *J. Geophys. Res.*, *112*(D10), D10103. doi: 10.1029/2006JD007781

Scholl, M. A., Shanley, J. B., Zegarra, J. P., & Coplen, T. B. (2009). The stable isotope amount effect: New insights from NEXRAD echo tops, Luquillo Mountains, Puerto Rico. *Water Resour. Res.*, *45*(12). doi: 10.1029/2008WR007515

Seibert, P., & Frank, A. (2004). Source-receptor matrix calculation with a Lagrangian particle dispersion model in backward mode. *Atmos. Chem. Phys.*, *4*(1), 51–63. doi: 10.5194/acp-4-51-2004

Simmonds, I., Keay, K., & Tristram Bye, J. A. (2011). Identification and climatology of Southern Hemisphere mobile fronts in a modern reanalysis. *J. Climate*, *25*(6), 1945–1962. doi: 10.1175/JCLI-D-11-00100.1

Skamarock, W. C., & Klemp, J. B. (2008). A time-split nonhydrostatic atmospheric model for weather research and forecasting applications. *Journal of Computational Physics*, *227*(7), 3465–3485. doi: 10.1016/j.jcp.2007.01.037

Smith, A., Massuel, S., Pollock, D., & Dillon, P. (2012). Geohydrology of the Tamala Limestone Formation in the Perth Region: Origin and role of secondary porosity.
doi: 10.4225/08/599dd0fd98a44

Sodemann, H., Aemisegger, F., Pfahl, S., Bitter, M., Corsmeier, U., Feuerle, T., ... Wernli, H. (2017). The stable isotopic composition of water vapour above Corsica during the HyMeX SOP1 campaign: Insight into vertical mixing processes from lower-tropospheric survey flights. *Atmospheric Chem. Phys.*, *17*(9), 6125–6151. doi: 10.5194/acp-17-6125-2017

Sodemann, H., Schwierz, C., & Wernli, H. (2008). Interannual variability of Greenland winter precipitation sources: Lagrangian moisture diagnostic and North Atlantic Oscillation influence. *J. Geophys. Res. Atmospheres*, *113*(D3). doi: 10.1029/2007JD008503

Steen-Larsen, H. C., Sveinbjörnsdottir, A. E., Peters, A. J., Masson-Delmotte, V., Guishard, M. P., Hsiao, G., ... White, J. W. C. (2014). Climatic controls on water vapor deuterium excess in the marine boundary layer of the North Atlantic based on 500 days of in situ, continuous measurements. *Atmos. Chem. Phys.*, *14*(15), 7741–7756. doi: 10.5194/acp-14-7741-2014

Stohl, A., Eckhardt, S., Forster, C., James, P., Spichtinger, N., & Seibert, P. (2002). A replacement for simple back trajectory calculations in the interpretation of atmospheric trace substance measurements. *Atmospheric Environment*, *36*(29), 4635–4648. doi: 10.1016/S1352-2310(02)00416-8

Sturm, K., Hoffmann, G., Langmann, B., & Stichler, W. (2005). Simulation of δ^{18}O in precipitation by the regional circulation model REMO_iso. *Hydrol. Process.*, *19*(17), 3425–3444. doi: 10.1002/hyp.5979

Treble, P. C., Bradley, C., Wood, A., Baker, A., Jex, C. N., Fairchild, I. J., ... Azcurra, C. (2013). An isotopic and modelling study of flow paths and storage in Quaternary calcarenite, SW Australia: Implications for speleothem paleoclimate records. *Quaternary Science Reviews*, *64*, 90–103. doi: 10.1016/j.quascirev.2012.12.015

Treble, P. C., Budd, W. F., Hope, P. K., & Rustomji, P. K. (2005). Synoptic-scale climate patterns associated with rainfall δ^{18}O in southern Australia. *J. Hydrol.*, *302*(1-4), 270–282. doi: 10.1016/j.jhydrol.2004.07.003

Treble, P. C., Chappell, J., Gagan, M. K., McKeegan, K. D., & Harrison, T. M. (2005). In situ measurement of seasonal δ^{18}O variations and analysis of isotopic trends in a modern speleothem from southwest Australia. *Earth and Planetary Science Letters*, *233*(1–2), 17–32. doi: 10.1016/j.epsl.2005.02.013

Tyler, J. J., Jones, M., Arrowsmith, C., Allott, T., & Leng, M. J. (2016). Spatial patterns in the oxygen isotope composition of daily rainfall in the British Isles. *Clim. Dyn.*, *47*(5-6), 1971–1987. doi: 10.1007/s00382-015-2945-y

Uemura, R., Matsui, Y., Yoshimura, K., Motoyama, H., & Yoshida, N. (2008). Evidence of deuterium excess in water vapor as an indicator of ocean surface conditions. *J. Geophys. Res. Atmospheres*, *113*(D19), D19114. doi: 10.1029/2008JD010209

van Breukelen, M. R., Vonhof, H. B., Hellstrom, J. C., Wester, W. C. G., & Kroon, D. (2008). Fossil dripwater in stalagmites reveals Holocene temperature and rainfall variation in Amazonia. *Earth and Planetary Science Letters*, *275*(1), 54–60. doi: 10.1016/j.epsl.2008.07.060

van Ommen, T. D., & Morgan, V. (2010). Snowfall increase in coastal East Antarctica linked with southwest Western Australian drought. *Nat. Geosci.*, *3*(4), 267–272. doi: 10.1038/ngeo761

Viney, N. R., & Bates, B. C. (2004). It never rains on Sunday: The prevalence and implications of untagged multi-day rainfall accumulations in the Australian high quality data set. *Int. J. Climatol.*, *24*(9), 1171–1192. doi: 10.1002/joc.1053

Vonhof, H. B., van Breukelen, M. R., Postma, O., Rowe, P. J., Atkinson, T. C., & Kroon, D. (2006). A continuous-flow crushing device for on-line δ^2H analysis of fluid inclusion water in speleothems. *Rapid Commun. Mass Spectrom.*, *20*(17), 2553–2558. doi: 10.1002/rcm.2618

Wang, S., Zhang, M., Crawford, J., Hughes, C. E., Du, M., & Liu, X. (2017). The effect of moisture source and synoptic conditions on precipitation isotopes in arid central Asia. *J. Geophys. Res. Atmos.*, 2015JD024626. doi: 10.1002/2015JD024626

Werner, M., Langebroek, P. M., Carlsen, T., Herold, M., & Lohmann, G. (2011). Stable water isotopes in the ECHAM5 general circulation model: Toward high-resolution isotope modeling on a global scale. *J. Geophys. Res.*, *116*(D15), D15109. doi: 10.1029/2011JD015681

Winnick, M. J., Chamberlain, C. P., Caves, J. K., & Welker, J. M. (2014). Quantifying the isotopic 'continental effect'. *Earth and Planetary Science Letters*, *406*, 123–133. doi: 10.1016/j.epsl.2014.09.005

Wood, S. N. (2011). Fast stable restricted maximum likelihood and marginal likelihood estimation of semiparametric generalized linear models. *J. R. Stat. Soc. Ser. B Stat. Methodol.*, *73*(1), 3–36. doi: 10.1111/j.1467-9868.2010.00749.x

Wood, S. N. (2017). *Generalized additive models: An introduction with R*. Chapman and Hall/CRC.

Xia, Z., & Winnick, M. J. (2021). The competing effects of terrestrial evapotranspiration and raindrop re-evaporation on the deuterium excess of continental precipitation. *Earth and Planetary Science Letters*, *572*, 117120. doi: 10.1016/j.epsl.2021.117120

Xu, X., Werner, M., Butzin, M., & Lohmann, G. (2012). Water isotope variations in the global ocean model MPI-OM. *Geosci. Model Dev.*, *5*(3), 809–818. doi: 10.5194/gmd-5-809-2012

Yoshimura, K., Kanamitsu, M., Noone, D., & Oki, T. (2008). Historical isotope simulation using Reanalysis atmospheric data. *J. Geophys. Res.*, *113*(D19), D19108. doi: 10.1029/2008JD010074

Zhang, H., Griffiths, M. L., Chiang, J. C. H., Kong, W., Wu, S., Atwood, A., ... Xie, S. (2018). East Asian hydroclimate modulated by the position of the westerlies during Termination I. *Science*, *362*(6414), 580–583. doi: 10.1126/science.aat9393

Zhang, Z., Li, G., Yan, H., & An, Z. (2018). Microcodium in Chinese loess as a recorder for the oxygen isotopic composition of monsoonal rainwater. *Quaternary International*, *464*, 364–369. doi: 10.1016/j.quaint.2017.10.050

Zheng, Y., Jong, L. M., Phipps, S. J., Roberts, J. L., Moy, A. D., Curran, M. A. J., & van Ommen, T. D. (2021). Extending and understanding the South West Western Australian rainfall record using a snowfall reconstruction

from Law Dome, East Antarctica. *Clim. Past*, *17*(5), 1973–1987. doi: 10.5194/cp-17-1973-2021